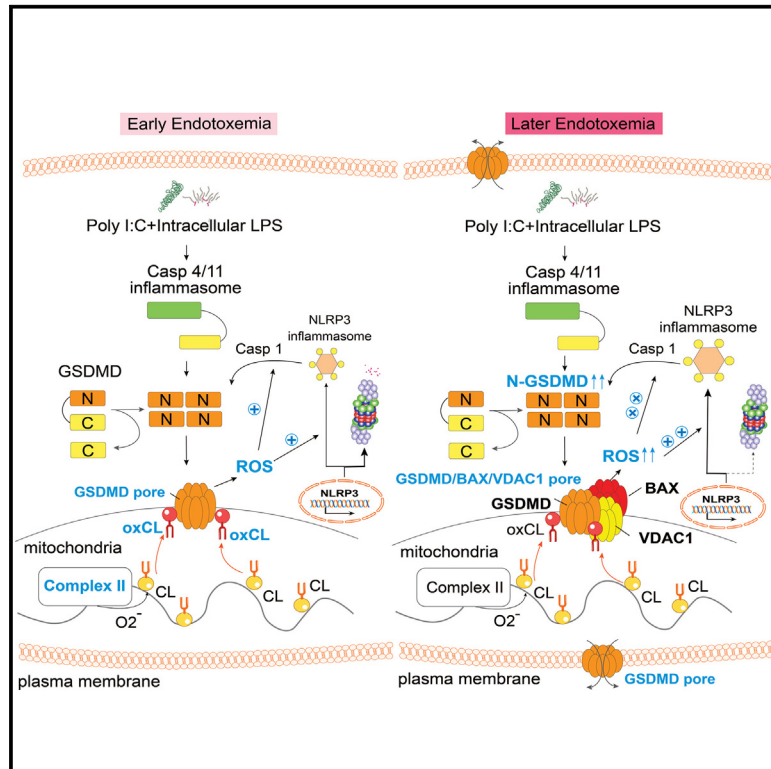**Article**

Cardiolipin oxidized by ROS from complex II acts as a target of gasdermin D to drive mitochondrial pore and heart dysfunction in endotoxemia

Graphical abstract

Authors

Yan Tang, Junru Wu, Xuejing Sun, ..., Qingbo Xu, Timothy R. Billiar, Jingjing Cai

Correspondence

caijingjing@csu.edu.cn

In brief

The mechanism that initiates cardiac dysfunction during endotoxemia remains unknown. Tang et al. show that GSDMD-N triggers early mitochondrial pore and heart dysfunction directly via oxidized cardiolipin by complex II in cardiomyocytes. Such pores further incorporate into BAX and VDAC1 oligomers to exacerbate the apoptotic process in cardiomyocytes.

Highlights

- GSDMD-N forms mitochondrial pores directly via oxidized cardiolipin in endotoxemia

- GSDMD pores form before BAX and VDAC apoptotic pores during cardiomyocyte death

- GSDMD-N oligomer-induced mROS release accelerates NLRP3 expression and activation

- Complex II is the major contributor to cardiolipin oxidation in cardiomyocytes

CellPress

Article

Cardiolipin oxidized by ROS from complex II acts as a target of gasdermin D to drive mitochondrial pore and heart dysfunction in endotoxemia

Yan Tang,[1,2] Junru Wu,[1] Xuejing Sun,[1] Shasha Tan,[1] Wenbo Li,[3] Siyu Yin,[1] Lun Liu,[1] Yuanyuan Chen,[1] Yuanyuan Liu,[1] Qian Tan,[1] Youxiang Jiang,[1] Wenjing Yang,[1] Wei Huang,[1] Chunyan Weng,[1] Qing Wu,[4] Yao Lu,[1] Hong Yuan,[1] Qingzhong Xiao,[5] Alex F. Chen,[1,6] Qingbo Xu,[7] Timothy R. Billiar,[8] and Jingjing Cai[1,9,*]

[1]Clinical Research Center, Department of Cardiology, the Third Xiangya Hospital, Central South University, Changsha 410013, China
[2]Department of Cardiology, The First Affiliated Hospital, Jiangxi Medical College, Nanchang University, Nanchang 330006, China
[3]Department of Plastic and Aesthetic (Burn) Surgery, the Second Xiangya Hospital, Central South University, Changsha 410000, China
[4]Center for High-Performance Computing, Central South University, Changsha 410000, China
[5]Centre for Clinical Pharmacology, William Harvey Research Institute, Barts, and The London School of Medicine and Dentistry, Queen Mary University of London, EC1M 6BQ London, UK
[6]Department of Cardiology, Institute for Cardiovascular Development and Regenerative Medicine, Xinhua Hospital Affiliated to Shanghai Jiao Tong University School of Medicine, 200092 Shanghai, China
[7]Department of Cardiology, the First Affiliated Hospital, Zhejiang University School of Medicine, Hangzhou 310003, China
[8]Department of Surgery, University of Pittsburgh Medical Center, Pittsburgh, PA 15213, USA
[9]Lead contact
*Correspondence: caijingjing@csu.edu.cn
https://doi.org/10.1016/j.celrep.2024.114237

SUMMARY

Cardiac dysfunction, an early complication of endotoxemia, is the major cause of death in intensive care units. No specific therapy is available at present for this cardiac dysfunction. Here, we show that the N-terminal gasdermin D (GSDMD-N) initiates mitochondrial apoptotic pore and cardiac dysfunction by directly interacting with cardiolipin oxidized by complex II-generated reactive oxygen species (ROS) during endotoxemia. Caspase-4/11 initiates GSDMD-N pores that are subsequently amplified by the upregulation and activation of NLRP3 inflammation through further generation of ROS. GSDMD-N pores form prior to BAX and VDAC1 apoptotic pores and further incorporate into BAX and VDAC1 oligomers within mitochondria membranes to exacerbate the apoptotic process. Our findings identify oxidized cardiolipin as the definitive target of GSDMD-N in mitochondria of cardiomyocytes during endotoxin-induced myocardial dysfunction (EIMD), and modulation of cardiolipin oxidation could be a therapeutic target early in the disease process to prevent EIMD.

INTRODUCTION

Endotoxemia and sepsis remain common causes for morbidity and mortality worldwide.[1] Systemic endotoxemia is also induced by an acute viral infection, including COVID-2019, Middle East Respiratory Syndrome, and H1N1 (swine flu), via translocation of bacterial products, such as lipopolysaccharide (LPS), from the gut into the circulation.[2] Endotoxemia can lead to the damage and dysfunction of multiple organs; however, myocardial dysfunction is the most common and earliest complication, and a decline in cardiac efficiency can contribute to the dysfunction of other organ systems.[3,4] Endotoxin-induced myocardial dysfunction (EIMD) can increase the mortality of patients by about 50%–70%.[5,6] Unfortunately, there is no specific therapy available for EIMD on the market. Thus, elucidating the key mechanisms leading to EIMD is essential to develop novel therapeutic approaches to prevent and treat this critical cause of ICU morbidity and mortality.[7]

Current knowledge on the pathogenic paradigm for EIMD has led to efforts to develop a therapeutic strategy around maintaining and restoring mitochondrial function, blocking inflammation, or preventing cell death. However, these strategies have not achieved satisfactory outcomes.[3,8–10] The heart has a high energy demand and continuously produces large amounts of ATP from mitochondria to sustain contractile function.[11] Since mitochondrial dysfunction leads to cardiac dysfunction at the very early phase of endotoxemia, we focused on defining the processes responsible for the earliest phases of mitochondrial dysfunction in cardiac myocytes.

Gasdermin D (GSDMD) is the critical effector of pyroptosis through a process where the cleaved N-terminal domain (GSDMD-N) inserts into the inner leaflet of plasma membranes, aggregates, and forms pores.[12–15] Recently, studies showed that GSDMD-N also permeabilizes the mitochondrial membrane to activate apoptosis in immune and endothelial cells.[14–18] However, the molecular target of GSDMD-N in mitochondrial
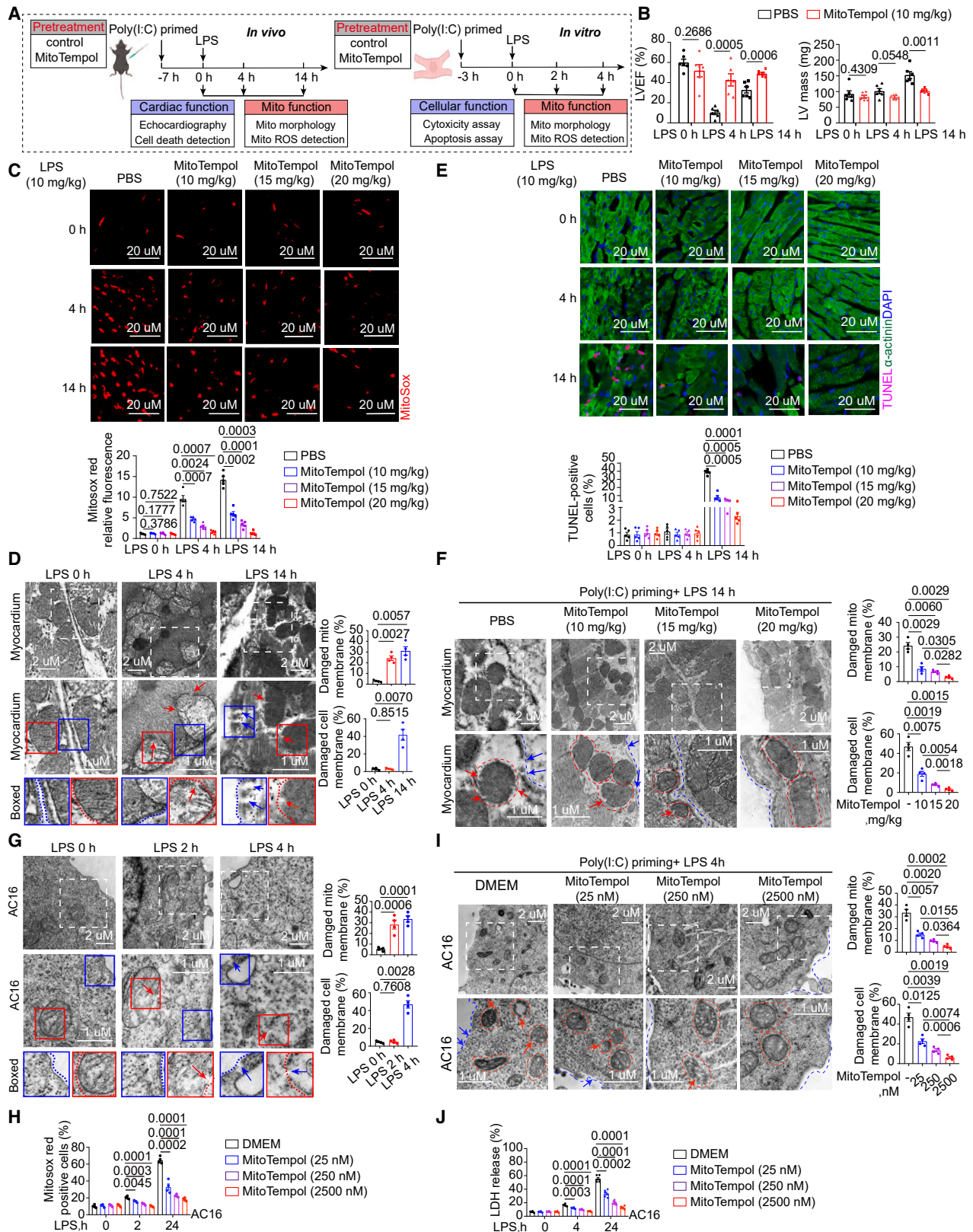
(legend on next page)

membranes has not been identified. Cardiolipin (CL) is a complex lipid present only in mitochondria (mainly in the inner membranes) in mammalian cells. Oxidation of CL leads to its redistribution from the inner mitochondrial membrane (IMM) to the outer mitochondrial membrane (OMM) under stress, where it mediates the formation of Bax/Bak pores in neuroblastoma cells and hepatocytes.[19–21] However, a detailed mechanism of how CL oxidization activates programmed cell death in cardiomyocytes during EIMD remains unknown.

In this study, we found that the pyrolytic executioner form of GSDMD forms early mitochondrial pores by interacting with oxidized CL (oxCL) in the OMM. This occurs prior to BAX and VDAC1 apoptotic pore formation and cytomembrane damage. Meanwhile, we showed that the predominant contributor to CL oxidation is reactive oxygen species (ROS) generated from complex II in cardiomyocytes. These findings link early metabolic stress with the initiation and propagation of mitochondrial dysfunction through a step that involves GSDMD-CL interaction.

RESULTS

Endotoxin induces early mitochondrial stress-associated cardiac dysfunction independent of cardiomyocyte death

We examined the functional changes in cardiomyocytes and mitochondria over time to determine the critical triggers for cardiac dysfunction during "double-hit" endotoxin challenges (Figure 1A).[22–24] The echocardiographic analysis revealed that cardiac function, as measured by left ventricular (LV) ejection fraction and LV fractional shortening, were substantially suppressed after a 4-h LPS challenge in wild-type (WT) mice (Figures 1B and S1A). Estimated LV mass, LV posterior wall thickness at end-diastole, and LV anterior wall thickness at end-diastole remained unchanged up to 8 h, but markedly increased after 14 h of LPS treatment compared with the baseline. This indicates progressive damage and edema in cardiomyocytes (Figure S1A; Table S1). Therefore, we used 4- and 14-h LPS exposure as early and late stages of EIMD, respectively. By assessing the changes in subcellular organelles over time, we found functional and morphological changes in mitochondria begin quickly after endotoxin exposure *in vivo* and *in vitro*. MitoSOX red and dihydroethidium staining showed massive production of ROS from mitochondria at 4 and 14 h after endotoxin challenge in the heart (Figures 1C, S1B, and S1C). Transmission electron microscopy (TEM) showed mitochondrial membrane damage in cardiomyocytes in heart tissue were also observed at 4 and 14 h after LPS stimulation (Figure 1D), while

cell membrane damage could only be detected at 14 h after LPS treatment (Figures 1D and S1D). Consistently, LPS challenge for 14 h induced significant cardiomyocyte death in heart tissue, a finding not observed at 4 h (Figure 1E). These findings indicate that endotoxin induces cardiac dysfunction by 4 h independent of cardiomyocyte death.

To test whether mitochondrial ROS (mROS) production initiates cardiac dysfunction in endotoxemia, we used MitoTempol, a specific mROS scavenger, in our murine model of EIMD. MitoTempol pretreatment (10–20 mg/kg) dose dependently prevented LPS-induced cardiac dysfunction (Figure 1B; Table S1) and mROS production (Figure 1C) at 4 h. Subsequently, MitoTempol reduced LPS-induced mitochondrial and cell membrane damage by TEM and cell death by TUNEL staining in cardiomyocytes at 14 h (Figures 1E and 1F).

We also determined whether LPS caused cardiomyocyte damage via mROS *in vitro* (Figures S1E and S1F).[16,18,22] Exposure of AC16 human cardiomyocytes to 1 μg/mL poly(I:C) followed by 10 ng/mL LPS for 2 h initiated mROS production (Figure S1G). Significant cell death was not observed until 4 h after LPS challenge, as detected by a lactate dehydrogenase assay (Figure S1H). Mitochondrial membrane damage was observed by TEM at 2 h after LPS with poly(I:C) priming and plasma membrane damage first appeared at 4 h (Figure 1G). Consistent with the *in vivo* observations, MitoTempol from 25 nM to 2.5 μM dose dependently reversed endotoxin-induced mROS production (Figure 1H), mitochondrial and cell membrane damage (Figures 1I and S1G), and cell death (Figures 1J, S1H, and S1I) at 4 h.

Thus, these findings support the key roles of mitochondrial oxidative stress and mitochondrial membrane damage in promoting early cardiac dysfunction and subsequent cardiomyocyte death under endotoxemia.

GSDMD oligomerization facilitates mitochondrial membrane damage and cardiac dysfunction in early endotoxemia

We further explored the early mechanisms that mediate mitochondrial membrane damage in EIMD. We found that GSDMD was cleaved in the myocardium at 4 and 14 h after LPS exposure *in vivo* and the major proportion of GSDMD-N was enriched and localized with mitochondria (Figure 2A). Native gel electrophoresis revealed that GSDMD-N oligomerized in the mitochondrial membrane by 4 h after LPS challenge, which was before GSDMD-N plasma membrane pores could be detected (Figure 2B). The proportion of GSDMD-N in the cytoplasm increased with the length of LPS exposure (Figure S2A), and the GSDMD-N

Figure 1. Endotoxin induces early mitochondrial stress-associated cardiac dysfunction independent of cardiomyocyte death

(A) Schematic of the experimental strategy.

(B–J) (B) The change of left ventricular ejection fraction (LVEF) and LV mass by echocardiography in the indicated groups (n = 6). Representative images of immunofluorescent staining of MitoSOX red (C) and TUNEL (E) in heart sections from wild-type (WT) mice treated with PBS or MitoTempol (10, 15, or 20 mg/kg) in the indicated groups (n = 5). Scale bars, 20 μm (MitoSOX red and TUNEL image). Mitochondrial and cell membrane damage by transmission electron microscopy (TEM) in heart sections from mice in the indicated groups (n = 4) (D and F) and AC16 cells (n = 4 independent experiments) (G and I) in the indicated groups. Red arrows indicate mitochondrial damage. Blue arrows indicate cell membrane damage. The red dashed line indicates the outer mitochondrial membrane and the blue dashed line indicates the outer cell membrane (D, F, G, and I). Scale bars, 2 μm (top) and 1 μm (bottom). (H) MitoSOX red density of AC16 by flow cytometry with the indicated treatments (n = 4 independent experiments). (J) LDH level in the supernatants of AC16 cells in the indicated groups (n = 6 independent experiments). A two-tailed Student's t test (B), one-way ANOVA with Bonferroni post hoc analysis (C–J). See also Figure S1 and Table S1.
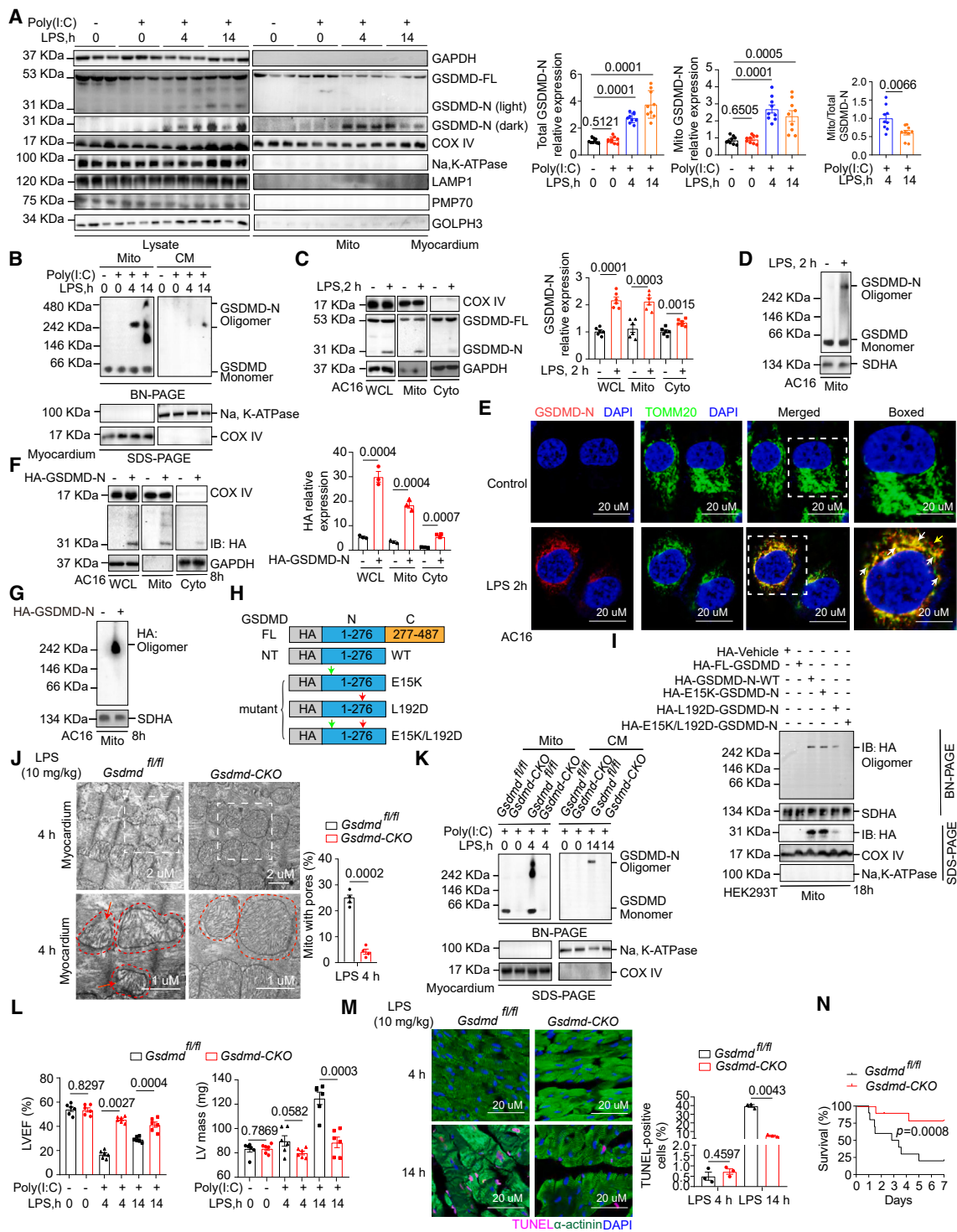
Figure 2. GSDMD oligomerization facilitates mitochondrial membrane damage and cardiac dysfunction in early endotoxemia

(A) SDS-PAGE analysis of GSDMD from whole-cell lysates (WCL) and mitochondrial (mito) fractions in the heart from WT mice in the indicated groups (*n* = 9).

(B) BN-PAGE analysis of GSDMD-N oligomers from mitochondrial and cell membrane (CM) in the heart from the indicated groups (*n* = 6).

(C and D) (C) SDS-PAGE analysis of GSDMD-N expression from WCL, mito, and cytosol and (D) BN-PAGE analysis of GSDMD-N oligomers from mitochondria in AC16 cells with the indicated groups (*n* = 4 independent experiments).

(legend continued on next page)

oligomer was detectable both in the mitochondrial and plasma membranes at 14 h after LPS stimulation (Figure 2B). In line with the observations *in vivo*, we also found that GSDMD-N oligomerized in mitochondria in AC16 cells and primary neonatal rat cardiomyocytes at 2 h LPS exposure (Figures 2C–2E and S2B). Together, these data demonstrate that oligomerized GSDMD-N is enriched in the mitochondrial membrane prior to the plasma membrane in cardiomyocytes during endotoxemia.

To further test whether GSDMD-N oligomerization is the key to early mitochondrial membrane damage, we overexpressed full-length gasdermin D (GSDMD-FL) and GSDMD-N by transfecting corresponding plasmids into HEK293T cells. Overexpression of GSDMD-N, but not GSDMD-FL, triggered GSDMD-N accumulation (Figure S2C), oligomerization (Figure S2D), and membrane damage (Figure S2E) in mitochondria of HEK293T cells at 18 h, without inducing cell death. Transfection of exogenous GSDMD-N for 18 h induced mitochondrial oxidative stress in the absence of cell death, as confirmed by measuring LDH release and mROS (Figures S2F and S2G). Similar results were obtained from AC16 cells overexpressing GSDMD-N (Figures 2F, 2G, and S2H–S2J). Combined, our results demonstrate that both endogenous and exogenous GSDMD-N primarily target mitochondria to form oligomers initiating mitochondrial membrane damage during endotoxemia.

We confirmed previous work showing that mutation of leucine 192 to aspartate (L192D) or glutamic acid 15 to lysine (E15K) in GSDMD-N can inhibit pore formation and pyroptosis (Figure 2H).[12] To extend our analysis to determine whether these residues of GSDMD-N are essential for its oligomerization in mitochondria, we transfected L192D, E15K, or E15K/L192D mutants of GSDMD-N into HEK293T cells. The L192D-mutant GSDMD-N markedly reduced GSDMD-N enrichment and oligomerization in mitochondria in HEK293T cells. Compared with the L192D single mutation, double mutations (E15K/L192D) further inhibited the accumulation and oligomerization of GSDMD-N in mitochondria (Figures 2I and S2K). These findings indicate that GSDMD-N L192 residue is critical for oligomerization and formation of mitochondrial pores.

To further validate the role of GSDMD in mitochondrial pore formation in cardiomyocytes and cardiac dysfunction during endotoxemia *in vivo*, we exposed *Gsdmd* cardiomyocyte-specific knockout (*Gsdmd*^fl/fl^; *Myosin heavy chain 6*-Cre [*Myh6*-Cre]

[*Gsdmd-CKO*]) mice and *Gsdmd*^fl/fl^ mice to a double-hit of endotoxin. Compared with *Gsdmd*^fl/fl^ mice, *Gsdmd-CKO* mice exhibited a profound reduction in mitochondrial and cell membrane pore formation (Figures 2J, 2K, and S2L). Meantime, *Gsdmd* deficiency in cardiomyocytes significantly reversed LPS-induced mROS production (Figure S2M), cardiac dysfunction (Figure 2L; Table S2), and cell death in cardiomyocytes (Figure 2M). Moreover, *Gsdmd-CKO* mice survived longer than *Gsdmd*^fl/fl^ mice after the endotoxin challenge (Figure 2N).

In sum, these data suggest that GSDMD activation facilitates mitochondrial pore formation and cardiac dysfunction early after endotoxin exposure. Mitochondrial GSDMD pore formation precedes plasma membrane pore formation and cardiomyocyte cell death.

Caspase-4/11 initiates GSDMD activation prior to the NLRP3 inflammasome leading to cardiac dysfunction in endotoxemia

To explore the key mechanisms that induce GSDMD cleavage and cardiac dysfunction, we performed bulk RNA sequencing of heart tissue from mice with poly(I:C) priming alone or with endotoxin exposure. Principal-component analysis of gene expression showed that the samples clustered into the four treatment groups, including baseline, 7 h of poly(I:C) priming alone, poly(I:C) priming + 4 h LPS challenge, and poly(I:C) priming + 14 h LPS challenge (Figure 3A). Compared with the control group, the group with poly(I:C) priming expressed higher levels of genes representing oxidative stress and alteration in energetic metabolisms, such as *Nrros*, *Adipod*, *Duoxa1*, *Acod1*, *Sdhaf2*, and *Atpaf1*. The addition of 4 h of LPS after poly(I:C) priming led to massive increases in a subset of inflammatory genes, including *Il1b*, *Nlrp3*, *Casp1*, *Casp4/11*, *Gsdmd*, *Tlr4*, and *Tnfaip3* (Figures 3B and 3C). By 14 h after the LPS challenge, the inflammatory genes remained increased; however, proapoptotic genes, including Casp3, Casp8, Casp9, and Bcl2ala, continued to significantly increase in heart tissue (Figure 3B). Compared with WT mice, *Tlr4*^−/−^, *Casp11*^−/−^, *Nlrp3*^−/−^, *Casp1*^−/−^, and *Gsdmd*^−/−^ mice showed significant amelioration of cardiac dysfunction (Figures 3D and S3A; Table S2), mROS production (Figures 3E and S3B), and mitochondrial pore formation (Figures 3F and S3C) in response to 4-h LPS challenge after poly(I:C). Among these transgenic mice, *Gsdmd*^−/−^ mice

(E) Immunofluorescent images showing the co-localization of mitochondria (TOMM20, green) and GSDMD-N (red) in AC16 cells (*n* = 3 independent experiments). Scale bars, 20 μm. White arrows indicated the co-localization of GSDMD-N with mitochondria. Yellow arrows indicate that GSDMD-N is not co-localized with mitochondria.

(F and G) (F) SDS-PAGE analysis of HA-tag expression from WCL, cytosol, and mito and (G) BN-PAGE analysis of HA oligomers from mitochondria in AC16 cells transfected with indicated HA-tagged plasmids for 8 h (*n* = 3 independent experiments).

(H) A mutation scheme of human HA-tagged truncated GSDMD-N.

(I) BN-PAGE analysis showing HA oligomers from mitochondria of HEK293T cells transfected with indicated HA-tagged plasmids for 18 h (*n* = 4 independent experiments).

(J) Mitochondrial pores by TEM in heart from *Gsdmd*^fl/fl^ and cardiomyocyte-specific knockout (*Gsdmd-CKO*) mice (*n* = 4). Red arrows indicate mitochondrial pores. The red dashed line indicates the outer mitochondrial membrane. Scale bars, 2 μm (top) and 1 μm (bottom).

(K) BN-PAGE analysis of GSDMD-N oligomers from mitochondria and CM in heart from *Gsdmd*^fl/fl^ and *Gsdmd-CKO* mice with the indicated treatments (*n* = 4).

(L) Echocardiography measuring LVEF and LV mass in *Gsdmd*^fl/fl^ and *Gsdmd-CKO* mice (*n* = 6).

(M) TUNEL (red) staining of cardiomyocytes (α-actinin⁺, green) in heart from *Gsdmd*^fl/fl^ and *Gsdmd-CKO* mice (*n* = 3). Scale bars, 20 μm.

(N) Kaplan-Meier plots for *Gsdmd*^fl/fl^ and *Gsdmd-CKO* mice injected with poly(I:C) for 7 h followed by LPS (*n* = 10). A two-tailed Student's t test (B–D, F, G, J, L, and M), one-way ANOVA with Bonferroni post hoc analysis (I), two-way ANOVA with Bonferroni post hoc analysis (A), and log rank test (N). See also Figure S2 and Table S2.
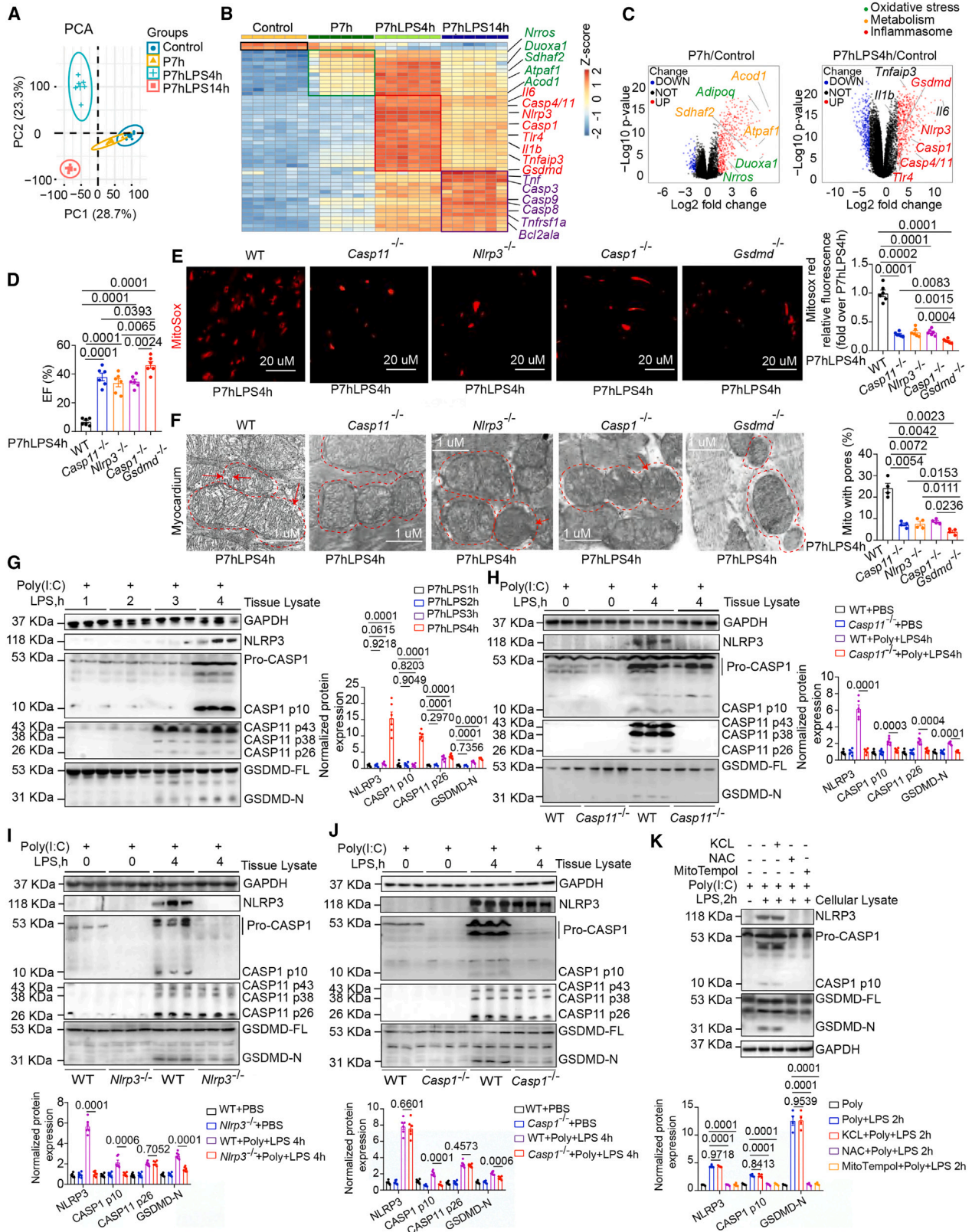
exhibited the best cardiac function (Figures 3D–3F). No significant difference in heart function between WT and these transgenic strains was observed at baseline (Figure S3D). *In vitro*, we used *TLR4* siRNA, *NLRP3* siRNA, *CASP4* siRNA, *CASP1* siRNA, and *GSDMD* siRNA for targeted gene knockdown in AC16 cardiomyocytes prior to poly(I:C) priming and followed by LPS treatment (Figure S3E). Silencing *NLRP3*, *CASP4*, *CASP1*, or *GSDMD* gene expression in AC16 cells reduced mROS and mitochondrial pore formation after 2 h of LPS exposure as well as cell death at 4 h following LPS challenge. Importantly, TLR4 deletion did not reverse these changes, implicating caspase-4 in cardiomyocyte LPS sensing (Figures S3F–S3H). This also suggests that the protective effect on cardiac function in TLR4$^{-/-}$ mice may be attributed to attenuating inflammatory responses in other cell types, such as macrophages and endothelial cells. Moreover, compared with AC16 with *CASP1* or *NLRP3* deficiency, AC16 with *CASP4* or *GSDMD* deficiency showed significant protection in the above-mentioned indicators, particularly at 14 h of LPS treatment (Figures S3F–S3H). Together, these results indicate that double-hit endotoxin exposure triggered both canonical and noncanonical inflammasome pathways in cardiomyocytes.

To identify which inflammasome activates first in EIMD, we performed the double-hit model and assessed inflammasome activation over time *in vivo* and *in vitro*. After poly(I:C) priming, heart tissue was harvested at 1, 2, 3, and 4 h after exposure to 10 mg/kg LPS. We observed that the noncanonical caspase-11 inflammasome was activated by 3 h, while the protein expression and activation of NLRP3 was observed at 4 h after LPS exposure (Figure 3G). Consistently, *Casp11*$^{-/-}$ mice showed significant amelioration of cardiac dysfunction (Figure 3D; Table S2), mROS production (Figure 3E), and mitochondrial pore formation (Figure 3F) in response to a 4-h LPS challenge. It is notable that the expression and activation of NLRP3 and CASP1, and the cleavage of GSDMD were markedly suppressed in *Casp11*$^{-/-}$ mice compared with WT mice after a 4-h LPS challenge (Figure 3H). The levels of cleaved GSDMD were partly inhibited in *Nlrp3*$^{-/-}$ and *Casp1*$^{-/-}$ mice compared with WT mice with endotoxemia, while CASP11 expression remained unchanged (Figures 3I and 3J). Similar results were observed in AC16 with LPS exposure (Figures S3I–S3L). Thus, caspase-4/11 activation precedes NLRP3/caspase-1 activation, which is partially driven by caspase-4/11 in the poly(I:C) priming + LPS stimulation model in the heart.

We further explored the mechanism that initiates NLRP3 priming and activation in LPS-treated cardiomyocytes. First, we blocked total ROS using N-acetylcysteine (NAC) (25 mM) or mROS using MitoTempol (2,500 nM), and both significantly blunted the level and activation of NLRP3 inflammasome following poly(I:C) priming + LPS stimulation (Figures 3K and S3M). Next, we assessed *NLRP3* mRNA expression using qPCR in the groups with NAC and MitoTempol and found that they did not inhibit poly(I:C) priming + LPS stimulation-induced *NLRP3* transcription (Figure S3N). We next tested if these ROS scavengers impact NLRP3 protein degradation. The proteasome inhibitor MG-132 reversed the ROS scavenger-related reduction in NLRP3 protein in poly(I:C) + LPS-treated AC16 cells (Figure S3O). In contrast, the lysosome inhibitor chloroquine did not change the NLRP3 protein level in poly(I:C) + LPS-treated AC16 cells in the presence of ROS scavengers (Figure S3P). These results indicate that ROS scavengers enhanced the degradation of NLRP3 via a proteasome-mediated mechanism in cardiomyocytes challenged with LPS (Figures S3O and S3P). Moreover, we found that MG-132 increased NLRP3 protein expression in cells with poly(I:C) priming alone, indicating the production of NLRP3 may be equivalent to its proteasomal degradation during poly(I:C) priming. These data may explain why NLRP3 protein is not expressed during the priming stage (Figures S3O and S3P). Since ubiquitin-mediated proteolysis plays an essential role in protein degradation and modification, we further explored if ubiquitination and the subsequent degradation process of NLRP3 proteins lead to its change during endotoxin exposure. Ubiquitination assays revealed that NLRP3 is ubiquitinated at baseline and during poly(I:C) priming in AC16 cells. At 2 h after poly(I:C) priming, NLRP3 protein was de-ubiquitinated. MitoTempol reversed poly(I:C) priming + LPS treatment induced NLRP3 protein de-ubiquitination (Figure S3Q).

Next, we constructed an NLRP3 knockout AC16 cell line that was reconstituted with NLRP3 protein to test if ROS scavengers directly inhibit NLRP3 activation. Application of H_2O_2 triggered NLRP3 activation, as shown by elevated caspase-1 cleavage, while MitoTempol inhibited H_2O_2-induced NLRP3 activation in NLRP3 knockout AC16 reconstituted with NLRP3 protein (Figure S3R). Importantly, inhibition of K$^+$ efflux using extracellular

---

Figure 3. Caspase-4/11 initiates GSDMD activation prior to the NLRP3 inflammasome leading to cardiac dysfunction in endotoxemia

(A) Principal-component analysis of bulk RNA sequencing data from heart tissue in the indicated mice groups ($n = 6$).

(B) Heatmap showing differentially expressed genes in heart tissue from the indicated groups.

(C) Volcano plot indicating transcriptomic changes in P7h group (left) and P7hLPS4h group (right) compared with the control group. The red and blue dots indicate upregulated and downregulated genes, respectively.

(D) Echocardiographic analysis of LVEF in WT, *Casp11*$^{-/-}$, *Nlrp3*$^{-/-}$, *Casp1*$^{-/-}$, and *Gsdmd*$^{-/-}$ mice with poly(I:C) for 7 h and LPS for 4 h ($n = 6$).

(E) MitoSOX red relative fluorescence in heart from the indicated groups ($n = 4$). Scale bars, 20 μm.

(F) Mitochondrial pores by TEM in heart with the indicated treatments ($n = 4$). Scale bars, 1 μm. Red arrows indicate mitochondrial pores. The red dashed line indicates the outer mitochondrial membrane.

(G) SDS-PAGE analysis of NLRP3, CASP1, CASP11, and GSDMD expression in heart tissue lysates from WT mice primed with poly(I:C) for 7 h followed by LPS for 1, 2, 3, or 4 h ($n = 6$).

(H–J) (H) SDS-PAGE analysis of NLRP3, CASP1, CASP11, and GSDMD expression in heart tissue lysates from WT or *Casp11*$^{-/-}$ mice ($n = 6$) and from WT or *Nlrp3*$^{-/-}$ mice ($n = 6$) and (I and J) from WT or *Casp1*$^{-/-}$ mice ($n = 6$) with the indicated treatments.

(K) SDS-PAGE analysis of NLRP3, CASP1, and GSDMD expression in cellular lysates from AC16 with the indicated treatments ($n = 4$ independent experiments).

One-way ANOVA with Bonferroni post hoc analysis (D–K), and two-way ANOVA with Bonferroni post hoc analysis (A–C). See also Figure S3 and Table S2.
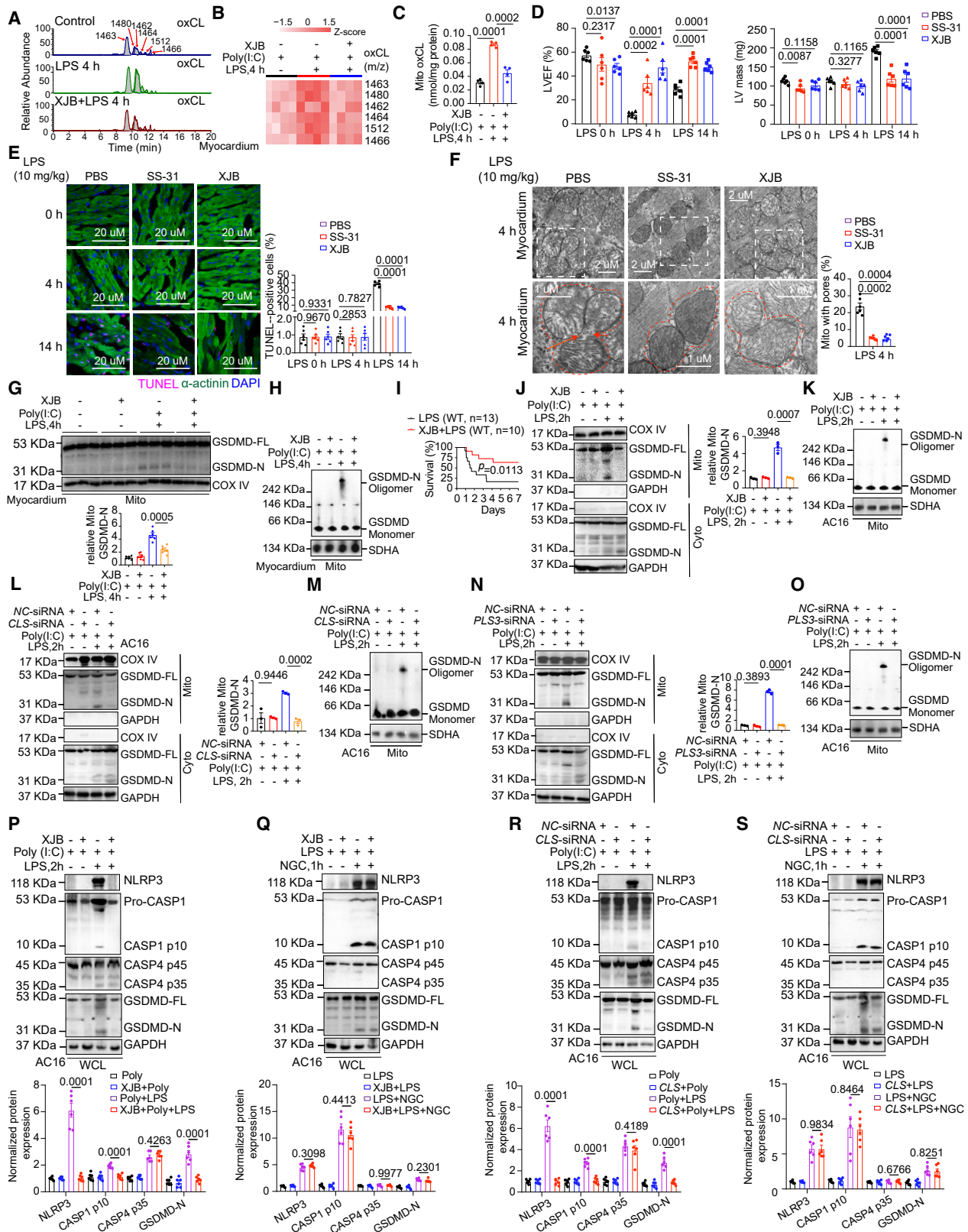
potassium chloride (KCL, 100 mM) did not inhibit NLRP3 inflammasome activation in response to LPS (Figure 3K). Nigericin is a pore-forming toxin that activates the NLRP3 inflammasome by stimulating an intracellular K^+ efflux.[25,26] Inhibition of mROS by MitoTempol did not inhibit LPS priming + nigericin-induced NLRP3 inflammasome expression and de-ubiquitination in AC16 cells (Figures S3S and S3T). Thus, this evidence suggests that the expression and activation of NLRP3 in cardiomyocytes may be induced by ROS following mitochondrial damage in response to LPS.

Collectively, our *in vitro* and *in vivo* data provide evidence that the caspase-4/11-GSDMD axis initiates mitochondrial damage and mROS release, and that this associates with further NLRP3-caspase-1 expression and activation in cardiomyocytes in response to LPS. mROS production in cardiomyocytes may increase NLRP3 expression by reducing its proteasome degradation and increasing NLRP3 activation. ROS scavenging blocks NLRP3 expression by enhancing its ubiquitination and proteasome degradation and also directly prevents its activation by ROS.

CL oxidation and externalization induce GSDMD-N oligomerization and pore formation in mitochondria

The oxidized form of CL redistributes from the IMM to the OMM, which is considered to be an essential signal for initiating apoptotic signaling.[27] Using ultra-high performance liquid chromatography-high-resolution tandem mass spectrometry (UHPLC-HRMS/MS) analysis, we quantified the levels of CL and oxCL in mitochondria after a 4-h LPS challenge. We identified 71 individual molecular species of CL in the mitochondria of cardiomyocytes, among which 6 were oxidized forms (Table S3). The quantities of total oxCLs were significantly increased with a 4-h LPS challenge compared with that at baseline, while the total amounts of CL did not change (Figures 4A–4C and S4A). Further, treatment with XJB-5-131, a conjugate of 4-amino-TEMPO and CL oxidation inhibitor, blocked endotoxin-induced oxCL accumulation (Figures 4A–4C and S4A) *in vitro*, and cardiac dysfunction (Figure 4D; Table S4), cell death (Figure 4E), mROS production (Figure S4B), reduction in the mitochondrial membrane potential (Figure S4C), and mitochondrial membrane pore for-

mation (Figure 4F) in the *in vivo* poly(I:C) priming + LPS stimulation model. SDS-PAGE and BN-PAGE immunoblotting showed that LPS-induced GSDMD-N accumulation and oligomerization were inhibited by XJB-5-131 in mitochondrial homogenates from heart tissue (Figures 4G and 4H). Moreover, pretreatment with XJB-5-131 prevented lethality in endotoxemia (Figure 4I). Consistent with observations *in vivo*, we also observed that XJB-5-131 blocked GSDMD-N accumulation (Figure 4J) and oligomerization (Figure 4K) in mitochondria from AC16 cells after 2 h of LPS exposure. A mitochondria-targeted peptide SS-31, which selectively binds to CL to protect it from oxidation, had a similar cardio-protection effect to XJB-5-131 (Figures 4D–4F and S4D–S4G; Table S4). Taken together, these findings demonstrate that oxCL is the direct target for GSDMD-N recruitment and oligomerization in mitochondria to initiate mitochondrial pore and cardiac dysfunction in endotoxemia.

To test whether LPS-induced GSDMD-N oligomerization depends on CL in mitochondria, we utilized siRNA against CL synthase (CLS) and measured the localization and oligomerization of GSDMD-N in cardiomyocytes. The results showed that CLS knockdown significantly inhibited GSDMD-N enrichment and oligomerization in mitochondria in AC16 cells after 2 h of LPS exposure (Figures 4L–4M, S4H, and S4K–S4M). Then, to further explore whether CL externalization was required for GSDMD-mediated mitochondrial pore formation, we blocked CL redistribution by constructing an siRNA against phospholipid scramblase-3 (PLS3), a key mitochondrial enzyme responsible for CL translocation from the IMM to the OMM.[19,28] PLS3 siRNA transfection also markedly inhibited oligomerization of GSDMD-N in mitochondria in AC16 cells with a 2-h LPS challenge (Figures 4N–4O, S4H, and S4K–S4M). Furthermore, we also observed that CLS or PLS3 knockdown in AC16 profoundly inhibited LPS-induced GSDMD-N oligomerized in the plasma membrane (Figure S4I) and cell death (Figure S4J) at 4 h after LPS treatment. In sum, these data suggest that oxidization and redistribution of CL induce GSDMD-N oligomerization and pore formation in mitochondria during the early phase of EIMD.

We further tested whether the protective effect of blocking CL oxidation is related to an effect on inflammasome expression and activation. From our work presented above, we know that

Figure 4. Cardiolipin oxidation and externalization induce GSDMD-N oligomerization and pore formation in mitochondria

(A–C) Typical spectra (A), heatmap (B), and quantification (C) of oxidized cardiolipin (oxCL) by mass spectrometry analysis in mitochondria from heart in WT mice with the indicated treatments ($n = 4$). For the heatmap, each row represents an individual oxCL species.

(D) Echocardiographic analysis of LVEF and LV mass in WT mice treated with PBS, SS-31 (5 mg/kg), or XJB-5-131 (10 mg/kg) in the indicated groups ($n = 6$).

(E) TUNEL (red) staining of cardiomyocytes (α-actinin$^+$, green) in the heart with the indicated treatments ($n = 6$). Scale bars, 20 μm.

(F) Mitochondria pores observed by TEM in the heart from the indicated groups ($n = 6$). Scale bars, 2 μm (top) and 1 μm (bottom). Red arrows indicate mitochondria pores. The red dashed line indicates the outer mitochondrial membrane.

(G and H) (G) SDS-PAGE analysis of GSDMD-N expression and (H) BN-PAGE analysis of GSDMD-N oligomers from mitochondria in the heart from WT mice with the indicated treatments ($n = 6$).

(I) Kaplan-Meier plots of WT mice pretreated with XJB-5-131 (10 mg/kg) and followed by poly(I:C) priming + LPS challenge ($n = 10–13$).

(J and K) (J) SDS-PAGE analysis of GSDMD-N expression from mitochondria and cytosol and (K) BN-PAGE analysis of GSDMD-N oligomers from mitochondria in AC16 cells pretreated with XJB-5-131 (10 μM) in the indicated groups ($n = 3$ independent experiments).

(L–O) (L and N) SDS-PAGE analysis of GSDMD-N expression from mitochondria and cytosol and (M and O) BN-PAGE analysis of GSDMD-N oligomers from mitochondria in AC16 cells transfected with indicated siRNA ($n = 3$ independent experiments).

(P–S) SDS-PAGE analysis of NLRP3, CASP1, CASP4, and GSDMD expression in AC16 cells pretreated with XJB (10 μM) (P and Q) or transfected with *CLS*-siRNA (R and S) followed by poly(I:C) priming + LPS (10 ng/mL, 2 h) or LPS priming + NGC (5 μM, 1 h) exposure ($n = 6$ independent experiments). SDHA as a fractional control for mitochondria fraction (H, K, M, and O). A two-tailed Student's t test (D–F), two-way ANOVA with Bonferroni post hoc analysis (C, G, H, J, K, P, and Q), multi-factor ANOVA with Bonferroni post hoc analysis (L–O, R, and S), and log rank test (I). See also Figure S4 and Tables S3 and S4.
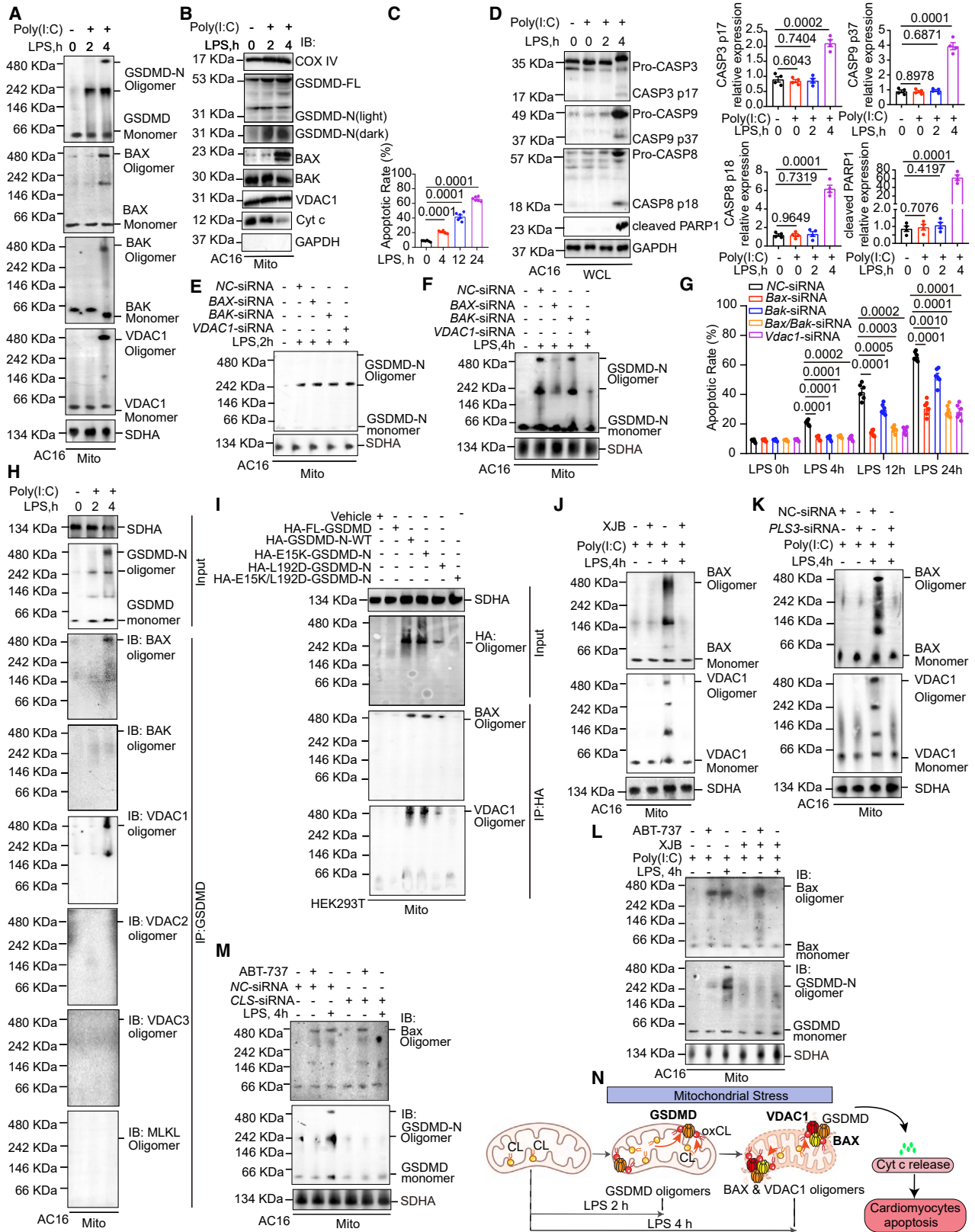
(legend on next page)

CASP11-GSDMD pathway activation precedes NLRP3-CASP1 activation at the 3-h time point after LPS treatment in poly(I:C)-primed mice (Figure 3G). In this model, XJB-5-131 significantly blocked GSDMD accumulation in the mitochondrial membrane but did not change levels of caspase-11 or GSDMD in whole-cell lysate (Figures S4N and S4O). Instead, XJB-5-131 effectively blocked the expression and activation of NLRP3, CASP1, and GSDMD in whole-cell lysate (Figure S4P), as well as GSDMD aggregation in the mitochondrial membrane at 4 h (Figure 4G). Therefore, we explored whether XJB-5-131 directly inhibited NLRP3-caspase-1-GSDMD axis in vitro. We showed that XJB-5-131 promoted NLRP3 proteasomal degradation and ubiquitination to suppress NLRP3 priming (Figures S4Q–S4S). XJB-5-131 also inhibited H_2O_2-triggered NLRP3 activation in NLRP3 knockout AC16 reconstituted with NLRP3 protein (Figure S4T). We also compared the effect of XJB-5-131 in cardiomyocytes with poly(I:C) + LPS treatment with that with LPS priming + nigericin treatment. XJB-5-131 significantly blocked poly(I:C) + LPS-induced NLRP3 expression and activation 2 h after the LPS challenge but did not inhibit nigericin-induced NLRP3 inflammasome expression and activation in cardiomyocytes (Figures 4P and 4Q). The observations in AC16 with CLS or PLS3 siRNA knockdown were consistent with the findings in AC16 with XJB-5-131 treatment (Figures 4R, 4S, and S4U–S4Z). This evidence indicates that CL oxidation and externalization mediate an increase in NLRP3 expression by reducing proteasome degradation, thereby enhancing NLRP3 activation in cardiomyocytes with LPS exposure.

GSDMD pore initially forms independent of BAX/BAK and VDAC pores in early endotoxemia

To further determine whether the mitochondrial GSDMD-N pore is independent of conventional apoptotic pores formed by BAX/BAK and VDAC1 in endotoxemia, we measured the expression of GSDMD-N, BAX, BAK, and VDAC1 oligomers and their interactions in mitochondria at various time points after LPS exposure in poly(I:C)-primed AC16 cells. The GSDMD-N oligomers were clearly evident after 2 h of LPS exposure, while appearance of BAX, BAK, and VDAC1 oligomers and cytochrome c release were not observed in the mitochondria of AC16 cells until 4 h af-

ter LPS treatment (Figures 5A and 5B). LPS-induced apoptosis (Annexin V-FITC$^+$) of AC16 cardiomyocytes increased from 21% at 4 h to 66% at 24 h after treatment (Figure 5C). In parallel, we observed that caspases responsible for executing apoptosis, including caspase-3, -8, and -9, were activated in AC16 by 4 h of LPS exposure (Figure 5D). Blocking BAX, BAK, and VDAC1 expression using siRNA transfection (Figure S5A), had no effect on LPS-induced GSDMD-N oligomerization in mitochondrial membrane at 2 h (Figures 5E and S5A), but did prevent the formation of the larger mitochondrial pores comprised of BAX and VDAC1 at 4 h (Figure 5F). It is notable that BAK deficiency did not inhibit GSDMD pore formation at either time point. Furthermore, deletion of BAX, BAK, BAX/BAK, or VDAC1 in AC16 cardiomyocytes had a protective effect on LPS-induced cell apoptosis at all time points. But, compared with AC16 cardiomyocytes with BAX, BAX/BAK, or VDAC1 deficiency, AC16 with BAK deficiency showed less protection in cell apoptosis at 12- and 24-h time points (Figure 5G). BN-PAGE analysis showed that BAK forms oligomers in the mitochondrial membrane. Pull-down experiments established that BAK does not directly interact with GSDMD pores in LPS-induced cell death, indicating that BAK oligomerization is independent of GSDMD pores (Figure 5H). In vivo, GSDMD-N oligomerization was observed after 4 h of LPS exposure, whereas BAX and VDAC1 oligomerization was not seen in heart mitochondrial homogenate until 14 h after LPS treatment (Figures S5B and S5C). Thus, we showed that the GSDMD-N oligomer appears earlier than BAX and VDAC1 oligomers in the mitochondria of cardiomyocytes during endotoxemia.

To determine the interactions among GSDMD-N, BAX, and VDAC1 proteins over time after endotoxin exposure, we performed co-immunoprecipitation assays in AC16 cells challenged with LPS. The results revealed that GSDMD-N oligomer did not interact with BAX or VDAC1 at the 2-h time point. However, interactions between GSDMD-N and BAX oligomers or between GSDMD-N and VDAC1 oligomers were observed in mitochondrial homogenates of AC16 cells at the 4-h time point (Figures 5H and S5D). In contrast, interactions between GSDMD-N and other channel proteins, such as BAK, VDAC2, VDAC3, and MLKL, were not found in AC16 cells at any time point after LPS

Figure 5. The GSDMD pore initially forms independent of BAX/BAK and VDAC pores in early endotoxemia

(A) BN-PAGE analysis of BAX, BAK, VDAC1, and GSDMD-N oligomers in mitochondria of AC16 cells with the indicated treatments (n = 6 independent experiments).

(B) SDS-PAGE analysis of GSDMD, BAX, BAK, VDAC1, and Cyt c expression in AC16 cells with the indicated groups (n = 4 independent experiments).

(C and G) Flow cytometry analysis showed the quantification of apoptotic AC16 cardiomyocytes (Annexin+) with the indicated treatments (n = 3–4 independent experiments).

(D) SDS-PAGE analysis of CASP3, CASP8, CASP9, and cleaved PARP1 expression in AC16 cells with the indicated groups (n = 4 independent experiments).

(E and F) BN-PAGE analysis of GSDMD-N oligomers from mitochondria in AC16 cells transfected with NC or indicated siRNA in the indicated groups (n = 4 independent experiments).

(H) Co-immunoprecipitation using an anti-GSDMD antibody were analyzed by BN-PAGE analysis for GSDMD-N, BAX, VDAC1, VDAC2, VDAC3, and MLKL oligomers from mitochondria of AC16 cells in the indicated treatments (n = 4 independent experiments).

(I) Co-immunoprecipitation assays of GSDMD-N, BAX, and VDAC1 oligomers in mitochondria from HEK293T cells transfected with indicated HA-tagged plasmids for 24 h (n = 4 independent experiments).

(J–M) BN-PAGE analysis of BAX and VDAC1 oligomers in mitochondria of AC16 cells pretreated with XJB (10 μM) (J) or transfected with PLS3-siRNA (K) in the indicated groups (n = 4 independent experiments). BN-PAGE analysis of BAX and GSDMD-N oligomers in AC16 cells pretreated with XJB-5-131(L) or transfected with indicated siRNA (M) and then challenged with ABT-737 (100 nM, 7 h) or poly(I:C) and LPS (10 ng/mL, 4 h) (n = 4 independent experiments).

(N) Schematic depicting the formation of mitochondrial GSDMD, BAX, and VDAC1 pores over the time of LPS exposure. SDHA as a fractional control for mitochondria fraction (A, F, H, and M). One-way ANOVA with Bonferroni post hoc analysis (I), two-way ANOVA with Bonferroni post hoc analysis (A, B, D, H, and J), and multi-factor ANOVA with Bonferroni post hoc analysis (E–G and K–M). See also Figure S5.
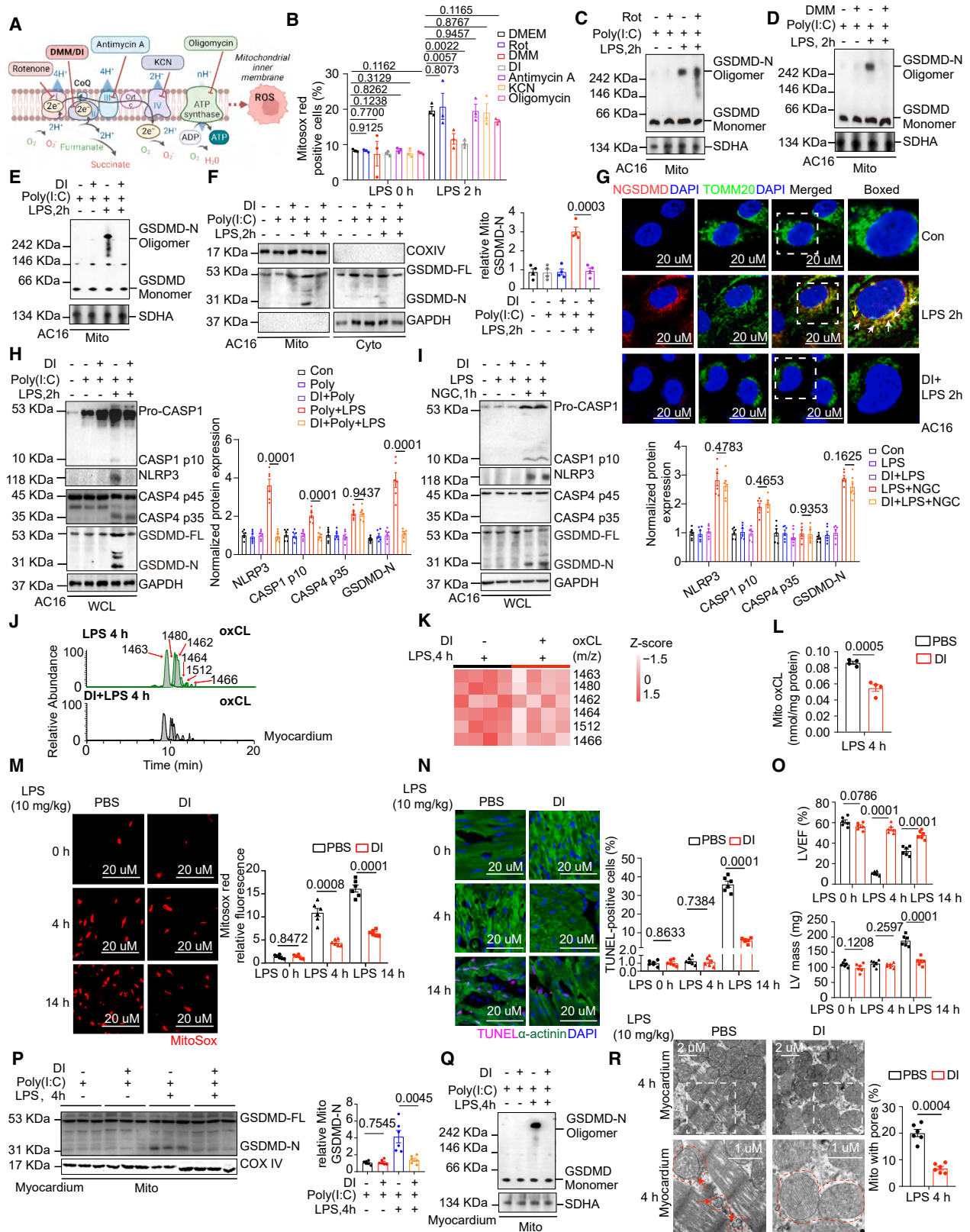
treatment (Figure 5H). We also established the delayed interaction of GSDMD-N oligomers with BAX and VDAC1 oligomers in the heart during endotoxemia (Figure S5E) and in HEK293T cells transfected with HA-tagged GSDMD-N plasmid and mutants (Figures 5I, S5F, and S5G). L192D or E15K/L192D mutants of GSDMD-N in HEK293T cells substantially suppressed mitochondrial BAX and VDAC1 oligomers (Figures 5I and S5G). These data suggest that GSDMD-N-mediated mitochondrial pores initiate and interact with mitochondrial apoptotic pores, such as BAX and VDAC1 pores, in the development of EIMD.

To further confirm whether oxidized and externalized CL is also the key target of mitochondrial GSDMD-N to trigger the BAX and VDAC1 pore formation in endotoxemia, we used XJB-5-131 or *PLS3* siRNA in AC16 cardiomyocytes with 4-h LPS stimulation. BN-PAGE immunoblotting revealed that XJB-5-131 (Figure 5J) or *PLS3* siRNA (Figure 5K) reduced the levels of BAX and VDAC1 oligomers in the mitochondria of cardiomyocytes after 4 h of LPS challenge. While XJB-5-131 or *CLS* siRNA treatment did not reduce the levels of BAX oligomers in the mitochondria of cardiomyocytes induced by BH3 mimetics (ABT-737, 100 nM) (Figures 5L and 5M).[29,30] These data support the conclusion that BAX oligomerization in cardiomyocytes during endotoxemia requires oxCL-induced GSDMD-N oligomerization in mitochondria (Figure 5N).

In sum, these data suggest that oxCL-induced GSDMD-N oligomers formed early and facilitated the interaction of L192 residue GSDMD-N with BAX and VDAC1 to form larger mitochondrial pores in the OMM after GSDMD-N pores have already formed.

Mitochondrial complex II is the major contributor to CL oxidation in cardiomyocytes

It has been previously reported that complexes of the electron transport chain (ETC) can generate ROS under stress conditions (Figure 6A).[31,32] To determine the potential source of mROS for the oxidation of CL, we tested selective inhibitors of the electron transport complexes in AC16 cells treated with LPS for 2 h. The elevation in mROS content was abolished only by pretreatment with complex II inhibitors, such as dimethyl itaconate (DI) or dimethyl malonate (DMM), indicating that complex II drove mROS production in cardiomyocytes during early endotoxemia

(Figure 6B). Importantly, GSDMD-N accumulation and oligomerization in mitochondria were also suppressed by the addition of complex II inhibitors, rather than inhibitors of other complexes 2 h after LPS treatment (Figures 6C–6F and S6A–S6D). The co-localization of GSDMD-N and the mitochondrial membrane (TOMM20) was decreased by the complex II inhibitor DI in AC16 cells during early endotoxemia (Figure 6G). Moreover, the application of DI inhibited cytosolic NLRP3 and CASP1 activation in AC16 with poly(I:C) + LPS treatment without changing CASP4 expression (Figure 6H). However, DI did not block nigericin-induced NLRP3 inflammasome activation in AC16 cells (Figure 6I). *In vivo* pretreatment with DI significantly attenuated mitochondrial oxCL levels (Figures 6J–6L and S6E; Table S3), mROS production (Figure 6M), loss of mitochondrial membrane potential (Figure S6F), cardiomyocyte apoptosis (Figure 6N), and cardiac dysfunction (Figure 6O; Table S4) after poly(I:C) priming + LPS exposure for 4 and 14 h in the murine model. Notably, GSDMD-N accumulation (Figures 6P and S6G), oligomerization (Figure 6Q), and membrane pore formation in mitochondria (Figure 6R) were suppressed by DI or DMM treatment in LPS-induced cardiac dysfunction *in vivo*. Therefore, our data provide evidence that mitochondrial complex II is a major contributor to CL oxidation in cardiomyocytes and to subsequent cardiac dysfunction.

DISCUSSION

The goal of this study was to define the early events driving mitochondrial dysfunction in cardiomyocytes exposed to endotoxin with a focus on the novel roles of GSDMD. We show that endotoxin promptly promotes noncanonical inflammasome-mediated GSDMD cleavage. Simultaneously, ROS generated by mitochondrial respiratory complex II oxidizes CL, which is externalized to the OMM. Cleaved GSDMD-N binds oxCL where it oligomerizes in the OMM forming pores. This occurs prior to the formation of GSDMD-N plasma membrane pores and prior to the formation of conventional pro-apoptotic BAX and VDAC1 pores in the OMM. GSDMD-N oligomer-mediated ROS release from mitochondria accelerates NLRP3 inflammasome expression and activation, which furthers mitochondria damage and cell death. Moreover, we provide insights into the mechanisms

Figure 6. Mitochondrial complex II is the major contributor to CL oxidation in cardiomyocytes during endotoxin exposure
(A) Schematic depicting respiratory chain complex.
(B) Quantitative results of MitoSOX red in AC16 cell with the indicated treatments (*n* = 3 independent experiments).
(C–E) BN-PAGE analysis of GSDMD-N oligomers in mitochondria of AC16 cells with the indicated treatments (*n* = 3 independent experiments).
(F) SDS-PAGE analysis of GSDMD expression from mitochondria and cytosol of AC16 cells with the indicated treatments (*n* = 3 independent experiments).
(G) Immunofluorescent images showing the co-localization of mitochondria (TOMM20, green) and GSDMD-N (red) in AC16 cells with the indicated treatments (*n* = 3 independent experiments). White arrows indicate the co-localization of GSDMD-N with mitochondria. Yellow arrows indicate that GSDMD-N is not co-localized with mitochondria. Scale bars, 20 μm.
(H–N) (H and I) SDS-PAGE analysis of NLRP3, CASP1, CASP4, and GSDMD expression in AC16 cells pretreated with the indicated treatments (*n* = 6 independent experiments). Typical spectra (J), heatmap (K), and quantification (L) of oxCL in heart mitochondria in WT mice with the indicated treatments (*n* = 4). Immunofluorescent staining of MitoSOX red (M) and TUNEL (red) (N) in heart from WT mice with the indicated treatments (*n* = 6). Scale bars, 20 μm.
(O) Echocardiography showing LVEF and LV mass in the indicated groups (*n* = 6).
(P and Q) (P) SDS-PAGE analysis of GSDMD-N expression and (Q) BN-PAGE analysis of GSDMD-N oligomers from heart mitochondria in the indicated groups (*n* = 6).
(R) TEM showing mitochondria pores in heart from WT mice with the indicated treatments (*n* = 6). Scale bars, 2 μm (top) and 1 μm (bottom). Red arrows indicate mitochondria pores. The red dashed line indicates the outer mitochondrial membrane. SDHA as a fractional control for mitochondria fraction (C–E and Q). A two-tailed Student's t test (L–O and R), and two-way ANOVA with Bonferroni post hoc analysis (B–F, H, I, P, and Q). See also Figure S6 and Tables S3 and S4.

behind the roles of mROS in the priming and activation of the NLRP3 inflammasome, which includes a suppression of NLRP3 degradation and direct activation of NLRP3 by mROS. The mechanistic insights gleaned from this work should inform efforts to prevent mitochondrial dysfunction during endotoxemia and potentially sepsis.

A recent study from Lieberman's team also reported a similar finding showing that GSDMD permeabilization of mitochondrial membranes via CL accelerates macrophage pyroptosis.[33] We observed similar findings in cardiomyocytes during endotoxemia and have extended findings as follows: first, we identified such GSDMD-N pores form prior to BAX and VDAC1 apoptotic pores and further incorporate into BAX and VDAC1 oligomers within mitochondria membranes to exacerbate the apoptotic process. Second, we showed that mitochondrial complex II is the main contributor to CL oxidation and initiates GSDMD-N pores in cardiomyocytes. Third, we found that mROS release enhances NLRP3 protein levels by inhibiting proteasomal degradation and its activation in cardiomyocytes.

GSDMD was first reported to act as a critical executioner of pyroptosis by inserting its N-terminal domain into the inner leaflet of the cell membrane and forming extensive pores.[12,13] Since then, the function of GSDMD and its associated mechanism have been actively studied.[12,17,34] In addition to being a key effector in pyroptotic cell death by forming pores in the plasma membrane, emerging evidence has shown that GSDMD-N permeabilizes the mitochondrial membrane to activate caspase-3-associated apoptosis or RIPK1/RIPK3/MLKL-dependent necroptosis in immune cells or to suppress YAP-mediated endothelial cell proliferation in response to different stimuli.[16,34] Since GSDMD pores permeabilize mitochondria and lead to the release of an array of mitochondrial damage-associated molecular patterns that trigger multiple cellular events, it is crucial to elucidate the direct targets of GSDMD-N on mitochondria and initiator of GSDMD cleavage during early injury. By combining *in vivo* and *in vitro* studies, we revealed that oxCL is the direct target of GSDMD-N on mitochondria in EIMD and that this is an initiating step that occurs prior to and is required for the formation of conventional mitochondrial apoptosis-induced channels, such as BAX and VDAC channels. Therefore, blocking the oxCL-GSDMD interaction could be a promising strategy for preventing and treating endotoxemia-related cardiac dysfunction.

Previous studies have shown that NLRP3 ubiquitination plays a critical role in the regulation of its degradation and this depends on the modification of different types of ubiquitin chains.[35–37] K48-linked ubiquitin chains serve as a signal for degradation by proteasomes, while K63-linked ubiquitin chains act as a signal for altering the functions of the modified protein, including signaling transduction, DNA repair, and intracellular trafficking.[38,39] K27-linked ubiquitination of NLRP3 induced by various E3 ubiquitin ligases leads to yet different effects on NLRP3 inflammasome degradation and activation.[35,40] We found that ROS production increases NLRP3 expression by reducing its ubiquitination and, hence, degradation, in cardiomyocytes with poly(I:C) priming + LPS treatment. However, the identification of the ubiquitin chains involved in ROS-related de-ubiquitination remains to be investigated in future studies. Moreover, we found that proteasome inhibition increased

NLRP3 protein expression with poly(I:C) priming alone, indicating that the production of NLRP3 may be equivalent to its proteasomal degradation during poly(I:C) priming. This evidence explains why NLRP3 protein is not expressed during priming.

CL is a tetra-acylated diphosphatidylglycerol lipid found in the mitochondrial membrane.[41] Under physiological conditions, CL is synthesized in the mitochondria by the enzyme CLS and resides in the IMM.[42,43] Pathogenic or proapoptotic stimuli can change the level of CL oxidation and generate various forms of oxCL. In addition, the activity of phospholipid-mobilizing enzymes, such as PLS3, is also upregulated to mediate the "flipping" of CL to the outer leaflet of the IMM and exposure of CL at the OMM during stimulation. Previous studies have shown that cytosol-exposed oxCL is an essential mediator of apoptosis, partially by recruiting tBID and forming BAX/BAK oligomers at the OMM.[21] Preclinical studies have shown that mild uncoupling of oxidative phosphorylation of mitochondria by XJB-5-131 leads to a reduction in CL oxidation and beneficial outcomes in traumatic brain injury and hemorrhagic shock.[44,45] In our study, we also observed that inhibition of CL oxidation or translocation attenuated BAX oligomerization in cardiomyocytes at the later phase of endotoxemia. More importantly, GSDMD-N formed pores with oxCL prior to the formation of BAX pores in this setting. Although studies have revealed that oligomeric BAX is sufficient to form small pores on liposomes and the OMM in the absence of CL,[46,47] GSDMD-N, or GSDMD-N-oxCL interaction markedly enhanced the process of mitochondrial apoptotic pore formation in our study. The detailed structure of this mitochondrial membrane channel requires cryoelectron microscopy examination in further studies.

The oxidation of CL and subsequent redistribution between the mitochondrial membranes depend on the production of ROS.[42,43] The mitochondrial ETC is a major source of ROS formation through continuous aerobic respiration that generates $O_2^{-\cdot}$.[48] Complexes I to V in the mitochondrial ETC are redox centers that transfer an electron to oxygen.[48] Complex I and complex III are the primary ROS generators in many cell types, including macrophages, T cells, and endothelial cells. In this study, we showed that complex II contributes to most ROS production for CL oxidation and apoptosis in cardiomyocytes during endotoxemia. One explanation for the high generation of ROS from complex II may be associated with reverse electron transfer from accumulated succinate to NAD+ in inflamed cells.[49,50] Mitochondrial fatty acid oxidation is the major source of energy for adult cardiomyocytes and a powerful source of FADH2.[51] The electron transfer from FADH2 potentiates the formation of ROS within complex II.[52] The elucidation of the source of ROS may reveal potential strategies for reducing cardiomyocyte damage during endotoxemia.

Limitations of the study

We acknowledge the limitations of our study. First, we focused on cardiomyocytes, while other heart cell types, such as fibroblasts, macrophages, and endothelial cells, may respond differently to endotoxin. Second, our mechanistic analysis was focused on mitochondrial GSDMD oligomerization and pore formation. Other gasdermin families identified in mitochondria should be further explored.[16] Third, although our study has

Cell Reports
Article

revealed that GSDMD-N targets oxidized CL to form mitochondrial pores and cardiac dysfunction during endotoxemia, other phospholipids potentially binding to GSDMD remain to be identified.

STAR★METHODS

Detailed methods are provided in the online version of this paper and include the following:

- KEY RESOURCES TABLE
- RESOURCE AVAILABILITY
  - Lead contact
  - Materials availability
  - Data and code availability
- EXPERIMENTAL MODEL AND STUDY PARTICIPANT DETAILS
  - Mouse studies
  - Endotoxin-induced myocardial dysfunction *in vivo*
  - Animal treatments and reagents
  - Cell lines culture
  - Culture of primary neonatal rat cardiomyocytes (NRCMs)
  - CRISPR/Cas9-mediated generation of NLRP3$^{-/-}$ AC16 cells
  - Endotoxin-induced cardiomyocyte injury *in vitro*
  - Cell treatments and reagents
- METHOD DETAILS
  - Echocardiography
  - Cardiac tissue harvest and preparation
  - Bulk RNA sequencing
  - Preparation of tissue subcellular fractions
  - Detection of ROS and mROS production in heart tissues
  - TUNEL staining and immunostaining in heart tissue
  - Quantification of CL and oxCL by UHPLC-HRMS/MS
  - Measurement of intracellular endotoxin levels
  - Plasmid transfection
  - Reconstitution of NLRP3 inflammasome in NLRP3$^{-/-}$ AC16 cells
  - siRNA transfection
  - mROS measurement using flow cytometry
  - JC-1 staining for mitochondrial membrane potential measurement
  - Apoptosis measurement using Annexin V/PI staining
  - Cytotoxicity assay
  - Confocal microscopy
  - Cellular ATP content
  - RNA extraction and RT–qPCR
  - Subcellular fractionation
  - Transmission electron microscopy
  - Antibodies
  - Western blot analysis
  - Blue Native-PAGE (BN-PAGE)
  - Co-immunoprecipitation (co-ip) assays
- QUANTIFICATION AND STATISTICAL ANALYSIS

SUPPLEMENTAL INFORMATION

Supplemental information can be found online at https://doi.org/10.1016/j.celrep.2024.114237.

DECLARATION OF INTERESTS

The authors declare no competing interests.

REFERENCES

1. Singer, M., Deutschman, C.S., Seymour, C.W., Shankar-Hari, M., Annane, D., Bauer, M., Bellomo, R., Bernard, G.R., Chiche, J.D., Coopersmith, C.M., et al. (2016). The Third International Consensus Definitions for Sepsis and Septic Shock (Sepsis-3). JAMA *315*, 801–810. https://doi.org/10.1001/jama.2016.0287.

2. Assimakopoulos, S.F., Eleftheriotis, G., Lagadinou, M., Karamouzos, V., Dousdampanis, P., Siakallis, G., and Marangos, M. (2022). SARS CoV-2-Induced Viral Sepsis: The Role of Gut Barrier Dysfunction. Microorganisms *10*, 1050. https://doi.org/10.3390/microorganisms10051050.

3. Hollenberg, S.M., and Singer, M. (2021). Pathophysiology of sepsis-induced cardiomyopathy. Nat. Rev. Cardiol. *18*, 424–434. https://doi.org/10.1038/s41569-020-00492-2.

4. Cecconi, M., Evans, L., Levy, M., and Rhodes, A. (2018). Sepsis and septic shock. Lancet *392*, 75–87. https://doi.org/10.1016/S0140-6736(18)30696-2.

5. Prescott, H.C., and Angus, D.C. (2018). Enhancing Recovery From Sepsis: A Review. JAMA *319*, 62–75. https://doi.org/10.1001/jama.2017.17687.

6. Landesberg, G., Gilon, D., Meroz, Y., Georgieva, M., Levin, P.D., Goodman, S., Avidan, A., Beeri, R., Weissman, C., Jaffe, A.S., and Sprung, C.L. (2012). Diastolic dysfunction and mortality in severe sepsis and septic shock. Eur. Heart J. *33*, 895–903. https://doi.org/10.1093/eurheartj/ehr351.

7. Zhang, Y.Y., and Ning, B.T. (2021). Signaling pathways and intervention therapies in sepsis. Signal Transduct. Target. Ther. *6*, 407. https://doi.org/10.1038/s41392-021-00816-9.

8. Martin, L., Derwall, M., Al Zoubi, S., Zechendorf, E., Reuter, D.A., Thiemermann, C., and Schuerholz, T. (2019). The Septic Heart: Current Understanding of Molecular Mechanisms and Clinical Implications. Chest *155*, 427–437. https://doi.org/10.1016/j.chest.2018.08.1037.

9. Abraham, E., Anzueto, A., Gutierrez, G., Tessler, S., San Pedro, G., Wunderink, R., Dal Nogare, A., Nasraway, S., Berman, S., Cooney, R., et al. (1998). Double-blind randomised controlled trial of monoclonal antibody

to human tumour necrosis factor in treatment of septic shock. NORASEPT II Study Group. Lancet *351*, 929–933.

10. Opal, S.M., and Yu, R.L. (1998). Antiendotoxin strategies for the prevention and treatment of septic shock. New approaches and future directions. Drugs *55*, 497–508. https://doi.org/10.2165/00003495-199855040-00002.

11. Bugger, H., Byrne, N.J., and Abel, E.D. (2022). Animal Models of Dysregulated Cardiac Metabolism. Circ. Res. *130*, 1965–1993. https://doi.org/10.1161/CIRCRESAHA.122.320334.

12. Ding, J., Wang, K., Liu, W., She, Y., Sun, Q., Shi, J., Sun, H., Wang, D.C., and Shao, F. (2016). Pore-forming activity and structural autoinhibition of the gasdermin family. Nature *535*, 111–116. https://doi.org/10.1038/nature18590.

13. Liu, X., Zhang, Z., Ruan, J., Pan, Y., Magupalli, V.G., Wu, H., and Lieberman, J. (2016). Inflammasome-activated gasdermin D causes pyroptosis by forming membrane pores. Nature *535*, 153–158. https://doi.org/10.1038/nature18629.

14. Liu, X., Xia, S., Zhang, Z., Wu, H., and Lieberman, J. (2021). Channelling inflammation: gasdermins in physiology and disease. Nat. Rev. Drug Discov. *20*, 384–405. https://doi.org/10.1038/s41573-021-00154-z.

15. Lieberman, J., Wu, H., and Kagan, J.C. (2019). Gasdermin D activity in inflammation and host defense. Sci. Immunol. *4*, eaav1447. https://doi.org/10.1126/sciimmunol.aav1447.

16. Rogers, C., Erkes, D.A., Nardone, A., Aplin, A.E., Fernandes-Alnemri, T., and Alnemri, E.S. (2019). Gasdermin pores permeabilize mitochondria to augment caspase-3 activation during apoptosis and inflammasome activation. Nat. Commun. *10*, 1689. https://doi.org/10.1038/s41467-019-09397-2.

17. Chen, K.W., Demarco, B., and Broz, P. (2020). Beyond inflammasomes: emerging function of gasdermins during apoptosis and NETosis. EMBO J. *39*, e103397. https://doi.org/10.15252/embj.2019103397.

18. Huang, L.S., Hong, Z., Wu, W., Xiong, S., Zhong, M., Gao, X., Rehman, J., and Malik, A.B. (2020). mtDNA Activates cGAS Signaling and Suppresses the YAP-Mediated Endothelial Cell Proliferation Program to Promote Inflammatory Injury. Immunity *52*, 475–486.e5. https://doi.org/10.1016/j.immuni.2020.02.002.

19. Chu, C.T., Ji, J., Dagda, R.K., Jiang, J.F., Tyurina, Y.Y., Kapralov, A.A., Tyurin, V.A., Yanamala, N., Shrivastava, I.H., Mohammadyani, D., et al. (2013). Cardiolipin externalization to the outer mitochondrial membrane acts as an elimination signal for mitophagy in neuronal cells. Nat. Cell Biol. *15*, 1197–1205. https://doi.org/10.1038/ncb2837.

20. Iriondo, M.N., Etxaniz, A., Varela, Y.R., Ballesteros, U., Hervás, J.H., Montes, L.R., Goñi, F.M., and Alonso, A. (2022). LC3 subfamily in cardiolipin-mediated mitophagy: a comparison of the LC3A, LC3B and LC3C homologs. Autophagy *18*, 2985–3003. https://doi.org/10.1080/15548627.2022.2062111.

21. Chen, L., Dong, J., Liao, S., Wang, S., Wu, Z., Zuo, M., Liu, B., Yan, C., Chen, Y., He, H., et al. (2022). Loss of Sam50 in hepatocytes induces cardiolipin-dependent mitochondrial membrane remodeling to trigger mtDNA release and liver injury. Hepatology *76*, 1389–1408. https://doi.org/10.1002/hep.32471.

22. Hagar, J.A., Powell, D.A., Aachoui, Y., Ernst, R.K., and Miao, E.A. (2013). Cytoplasmic LPS activates caspase-11: implications in TLR4-independent endotoxic shock. Science *341*, 1250–1253. https://doi.org/10.1126/science.1240988.

23. Kayagaki, N., Wong, M.T., Stowe, I.B., Ramani, S.R., Gonzalez, L.C., Akashi-Takamura, S., Miyake, K., Zhang, J., Lee, W.P., Muszyński, A., et al. (2013). Noncanonical inflammasome activation by intracellular LPS independent of TLR4. Science *341*, 1246–1249. https://doi.org/10.1126/science.1240248.

24. Sun, X., Wu, J., Liu, L., Chen, Y., Tang, Y., Liu, S., Chen, H., Jiang, Y., Liu, Y., Yuan, H., et al. (2022). Transcriptional switch of hepatocytes initiates macrophage recruitment and T-cell suppression in endotoxemia. J. Hepatol. *77*, 436–452. https://doi.org/10.1016/j.jhep.2022.02.028.

25. Muñoz-Planillo, R., Kuffa, P., Martínez-Colón, G., Smith, B.L., Rajendiran, T.M., and Núñez, G. (2013). K^+ efflux is the common trigger of NLRP3 inflammasome activation by bacterial toxins and particulate matter. Immunity *38*, 1142–1153. https://doi.org/10.1016/j.immuni.2013.05.016.

26. Yang, D., He, Y., Muñoz-Planillo, R., Liu, Q., and Núñez, G. (2015). Caspase-11 Requires the Pannexin-1 Channel and the Purinergic P2X7 Pore to Mediate Pyroptosis and Endotoxic Shock. Immunity *43*, 923–932. https://doi.org/10.1016/j.immuni.2015.10.009.

27. Hoye, A.T., Davoren, J.E., Wipf, P., Fink, M.P., and Kagan, V.E. (2008). Targeting mitochondria. Acc. Chem. Res. *41*, 87–97. https://doi.org/10.1021/ar700135m.

28. Huang, Z., Jiang, J., Tyurin, V.A., Zhao, Q., Mnuskin, A., Ren, J., Belikova, N.A., Feng, W., Kurnikov, I.V., and Kagan, V.E. (2008). Cardiolipin deficiency leads to decreased cardiolipin peroxidation and increased resistance of cells to apoptosis. Free Radic. Biol. Med. *44*, 1935–1944. https://doi.org/10.1016/j.freeradbiomed.2008.02.016.

29. Konopleva, M., Contractor, R., Tsao, T., Samudio, I., Ruvolo, P.P., Kitada, S., Deng, X., Zhai, D., Shi, Y.X., Sneed, T., et al. (2006). Mechanisms of apoptosis sensitivity and resistance to the BH3 mimetic ABT-737 in acute myeloid leukemia. Cancer Cell *10*, 375–388. https://doi.org/10.1016/j.ccr.2006.10.006.

30. Delbridge, A.R.D., Grabow, S., Strasser, A., and Vaux, D.L. (2016). Thirty years of BCL-2: translating cell death discoveries into novel cancer therapies. Nat. Rev. Cancer *16*, 99–109. https://doi.org/10.1038/nrc.2015.17.

31. Mills, E.L., Kelly, B., Logan, A., Costa, A.S.H., Varma, M., Bryant, C.E., Tourlomousis, P., Däbritz, J.H.M., Gottlieb, E., Latorre, I., et al. (2016). Succinate Dehydrogenase Supports Metabolic Repurposing of Mitochondria to Drive Inflammatory Macrophages. Cell *167*, 457–470.e13. https://doi.org/10.1016/j.cell.2016.08.064.

32. Hou, T., Zhang, R., Jian, C., Ding, W., Wang, Y., Ling, S., Ma, Q., Hu, X., Cheng, H., and Wang, X. (2019). NDUFAB1 confers cardio-protection by enhancing mitochondrial bioenergetics through coordination of respiratory complex and supercomplex assembly. Cell Res. *29*, 754–766. https://doi.org/10.1038/s41422-019-0208-x.

33. Miao, R., Jiang, C., Chang, W.Y., Zhang, H., An, J., Ho, F., Chen, P., Zhang, H., Junqueira, C., Amgalan, D., et al. (2023). Gasdermin D permeabilization of mitochondrial inner and outer membranes accelerates and enhances pyroptosis. Immunity *56*, 2523–2541.e8. https://doi.org/10.1016/j.immuni.2023.10.004.

34. Weindel, C.G., Martinez, E.L., Zhao, X., Mabry, C.J., Bell, S.L., Vail, K.J., Coleman, A.K., VanPortfliet, J.J., Zhao, B., Wagner, A.R., et al. (2022). Mitochondrial ROS promotes susceptibility to infection via gasdermin D-mediated necroptosis. Cell *185*, 3214–3231.e23. https://doi.org/10.1016/j.cell.2022.06.038.

35. Wang, D., Zhang, Y., Xu, X., Wu, J., Peng, Y., Li, J., Luo, R., Huang, L., Liu, L., Yu, S., et al. (2021). YAP promotes the activation of NLRP3 inflammasome via blocking K27-linked polyubiquitination of NLRP3. Nat. Commun. *12*, 2674. https://doi.org/10.1038/s41467-021-22987-3.

36. Song, H., Liu, B., Huai, W., Yu, Z., Wang, W., Zhao, J., Han, L., Jiang, G., Zhang, L., Gao, C., and Zhao, W. (2016). The E3 ubiquitin ligase TRIM31 attenuates NLRP3 inflammasome activation by promoting proteasomal degradation of NLRP3. Nat. Commun. *7*, 13727. https://doi.org/10.1038/ncomms13727.

37. Yan, Y., Jiang, W., Liu, L., Wang, X., Ding, C., Tian, Z., and Zhou, R. (2015). Dopamine controls systemic inflammation through inhibition of NLRP3 inflammasome. Cell *160*, 62–73. https://doi.org/10.1016/j.cell.2014.11.047.

38. Varadan, R., Walker, O., Pickart, C., and Fushman, D. (2002). Structural properties of polyubiquitin chains in solution. J. Mol. Biol. *324*, 637–647. https://doi.org/10.1016/s0022-2836(02)01198-1.

39. Deshaies, R.J., and Joazeiro, C.A.P. (2009). RING domain E3 ubiquitin ligases. Annu. Rev. Biochem. *78*, 399–434. https://doi.org/10.1146/annurev.biochem.78.101807.093809.

40. Guo, Y., Li, L., Xu, T., Guo, X., Wang, C., Li, Y., Yang, Y., Yang, D., Sun, B., Zhao, X., et al. (2020). HUWE1 mediates inflammasome activation and promotes host defense against bacterial infection. J. Clin. Invest. *130*, 6301–6316. https://doi.org/10.1172/JCI138234.

41. Kagan, V.E., Tyurin, V.A., Jiang, J., Tyurina, Y.Y., Ritov, V.B., Amoscato, A.A., Osipov, A.N., Belikova, N.A., Kapralov, A.A., Kini, V., et al. (2005). Cytochrome c acts as a cardiolipin oxygenase required for release of proapoptotic factors. Nat. Chem. Biol. *1*, 223–232. https://doi.org/10.1038/nchembio727.

42. Pizzuto, M., Pelegrin, P., and Ruysschaert, J.M. (2022). Lipid-protein interactions regulating the canonical and the non-canonical NLRP3 inflammasome. Prog. Lipid Res. *87*, 101182. https://doi.org/10.1016/j.plipres.2022.101182.

43. Pizzuto, M., and Pelegrin, P. (2020). Cardiolipin in Immune Signaling and Cell Death. Trends Cell Biol. *30*, 892–903. https://doi.org/10.1016/j.tcb.2020.09.004.

44. Ji, J., Kline, A.E., Amoscato, A., Samhan-Arias, A.K., Sparvero, L.J., Tyurin, V.A., Tyurina, Y.Y., Fink, B., Manole, M.D., Puccio, A.M., et al. (2012). Lipidomics identifies cardiolipin oxidation as a mitochondrial target for redox therapy of brain injury. Nat. Neurosci. *15*, 1407–1413. https://doi.org/10.1038/nn.3195.

45. Macias, C.A., Chiao, J.W., Xiao, J., Arora, D.S., Tyurina, Y.Y., Delude, R.L., Wipf, P., Kagan, V.E., and Fink, M.P. (2007). Treatment with a novel hemigramicidin-TEMPO conjugate prolongs survival in a rat model of lethal hemorrhagic shock. Ann. Surg. *245*, 305–314. https://doi.org/10.1097/01.sla.0000236626.57752.8e.

46. Lai, Y.C., Li, C.C., Sung, T.C., Chang, C.W., Lan, Y.J., and Chiang, Y.W. (2019). The role of cardiolipin in promoting the membrane pore-forming activity of BAX oligomers. Biochim. Biophys. Acta. Biomembr. *1861*, 268–280. https://doi.org/10.1016/j.bbamem.2018.06.014.

47. Kuwana, T., Mackey, M.R., Perkins, G., Ellisman, M.H., Latterich, M., Schneiter, R., Green, D.R., and Newmeyer, D.D. (2002). Bid, Bax, and lipids cooperate to form supramolecular openings in the outer mitochondrial membrane. Cell *111*, 331–342. https://doi.org/10.1016/s0092-8674(02)01036-x.

48. Zorov, D.B., Juhaszova, M., and Sollott, S.J. (2014). Mitochondrial reactive oxygen species (ROS) and ROS-induced ROS release. Physiol. Rev. *94*, 909–950. https://doi.org/10.1152/physrev.00026.2013.

49. Banerjee, R., and Kumar, R. (2022). Gas regulation of complex II reversal via electron shunting to fumarate in the mammalian ETC. Trends Biochem. Sci. *47*, 689–698. https://doi.org/10.1016/j.tibs.2022.03.011.

50. Hadrava Vanova, K., Kraus, M., Neuzil, J., and Rohlena, J. (2020). Mitochondrial complex II and reactive oxygen species in disease and pharmacology. Redox Rep. *25*, 26–32. https://doi.org/10.1080/13510002.2020.1752002.

51. Gaspar, J.A., Doss, M.X., Hengstler, J.G., Cadenas, C., Hescheler, J., and Sachinidis, A. (2014). Unique metabolic features of stem cells, cardiomyocytes, and their progenitors. Circ. Res. *114*, 1346–1360. https://doi.org/10.1161/CIRCRESAHA.113.302021.

52. Dröse, S. (2013). Differential effects of complex II on mitochondrial ROS production and their relation to cardioprotective pre- and postconditioning. Biochim. Biophys. Acta *1827*, 578–587. https://doi.org/10.1016/j.bbabio.2013.01.004.

53. Yang, X., Cheng, X., Tang, Y., Qiu, X., Wang, Y., Kang, H., Wu, J., Wang, Z., Liu, Y., Chen, F., et al. (2019). Bacterial Endotoxin Activates the Coagulation Cascade through Gasdermin D-Dependent Phosphatidylserine Exposure. Immunity *51*, 983–996.e6. https://doi.org/10.1016/j.immuni.2019.11.005.

54. Tang, Y., Wang, X., Li, Z., He, Z., Yang, X., Cheng, X., Peng, Y., Xue, Q., Bai, Y., Zhang, R., et al. (2021). Heparin prevents caspase-11-dependent septic lethality independent of anticoagulant properties. Immunity *54*, 454–467.e6. https://doi.org/10.1016/j.immuni.2021.01.007.

55. Xu, J., Jiang, Y., Wang, J., Shi, X., Liu, Q., Liu, Z., Li, Y., Scott, M.J., Xiao, G., Li, S., et al. (2014). Macrophage endocytosis of high-mobility group box 1 triggers pyroptosis. Cell Death Differ. *21*, 1229–1239. https://doi.org/10.1038/cdd.2014.40.

56. Patil, N.K., Parajuli, N., MacMillan-Crow, L.A., and Mayeux, P.R. (2014). Inactivation of renal mitochondrial respiratory complexes and manganese superoxide dismutase during sepsis: mitochondria-targeted antioxidant mitigates injury. Am. J. Physiol. Renal Physiol. *306*, F734–F743. https://doi.org/10.1152/ajprenal.00643.2013.

57. Zhao, Z., Wu, J., Xu, H., Zhou, C., Han, B., Zhu, H., Hu, Z., Ma, Z., Ming, Z., Yao, Y., et al. (2020). XJB-5-131 inhibited ferroptosis in tubular epithelial cells after ischemia-reperfusion injury. Cell Death Dis. *11*, 629. https://doi.org/10.1038/s41419-020-02871-6.

58. Liu, D., Jin, F., Shu, G., Xu, X., Qi, J., Kang, X., Yu, H., Lu, K., Jiang, S., Han, F., et al. (2019). Enhanced efficiency of mitochondria-targeted peptide SS-31 for acute kidney injury by pH-responsive and AKI-kidney targeted nanopolyplexes. Biomaterials *211*, 57–67. https://doi.org/10.1016/j.biomaterials.2019.04.034.

59. Lampropoulou, V., Sergushichev, A., Bambouskova, M., Nair, S., Vincent, E.E., Loginicheva, E., Cervantes-Barragan, L., Ma, X., Huang, S.C.C., Griss, T., et al. (2016). Itaconate Links Inhibition of Succinate Dehydrogenase with Macrophage Metabolic Remodeling and Regulation of Inflammation. Cell Metab. *24*, 158–166. https://doi.org/10.1016/j.cmet.2016.06.004.

60. Bambouskova, M., Gorvel, L., Lampropoulou, V., Sergushichev, A., Loginicheva, E., Johnson, K., Korenfeld, D., Mathyer, M.E., Kim, H., Huang, L.H., et al. (2018). Electrophilic properties of itaconate and derivatives regulate the IκBζ-ATF3 inflammatory axis. Nature *556*, 501–504. https://doi.org/10.1038/s41586-018-0052-z.

61. Miao, R., Lu, Y., Xing, X., Li, Y., Huang, Z., Zhong, H., Huang, Y., Chen, A.F., Tang, X., Li, H., et al. (2016). Regulator of G-Protein Signaling 10 Negatively Regulates Cardiac Remodeling by Blocking Mitogen-Activated Protein Kinase-Extracellular Signal-Regulated Protein Kinase 1/2 Signaling. Hypertension *67*, 86–98. https://doi.org/10.1161/HYPERTENSIONAHA.115.05957.

62. Sun, X., Zhou, M., Wen, G., Huang, Y., Wu, J., Peng, L., Jiang, W., Yuan, H., Lu, Y., and Cai, J. (2021). Paroxetine Attenuates Cardiac Hypertrophy Via Blocking GRK2 and ADRB1 Interaction in Hypertension. J. Am. Heart Assoc. *10*, e016364. https://doi.org/10.1161/JAHA.120.016364.

63. Ran, F.A., Hsu, P.D., Wright, J., Agarwala, V., Scott, D.A., and Zhang, F. (2013). Genome engineering using the CRISPR-Cas9 system. Nat. Protoc. *8*, 2281–2308. https://doi.org/10.1038/nprot.2013.143.

64. Ni, R., Cao, T., Xiong, S., Ma, J., Fan, G.C., Lacefield, J.C., Lu, Y., Le Tissier, S., and Peng, T. (2016). Therapeutic inhibition of mitochondrial reactive oxygen species with mitoTempol reduces diabetic cardiomyopathy. Free Radic. Biol. Med. *90*, 12–23. https://doi.org/10.1016/j.freeradbiomed.2015.11.013.

65. Zhao, K., Luo, G., Giannelli, S., and Szeto, H.H. (2005). Mitochondria-targeted peptide prevents mitochondrial depolarization and apoptosis induced by tert-butyl hydroperoxide in neuronal cell lines. Biochem. Pharmacol. *70*, 1796–1806. https://doi.org/10.1016/j.bcp.2005.08.022.

66. Matsuda, T., Zhai, P., Sciarretta, S., Zhang, Y., Jeong, J.I., Ikeda, S., Park, J., Hsu, C.P., Tian, B., Pan, D., et al. (2016). NF2 Activates Hippo Signaling and Promotes Ischemia/Reperfusion Injury in the Heart. Circ. Res. *119*, 596–606.

67. Platnich, J.M., Chung, H., Lau, A., Sandall, C.F., Bondzi-Simpson, A., Chen, H.M., Komada, T., Trotman-Grant, A.C., Brandelli, J.R., Chun, J., et al. (2018). Shiga Toxin/Lipopolysaccharide Activates Caspase-4 and Gasdermin D to Trigger Mitochondrial Reactive Oxygen Species Upstream of the NLRP3 Inflammasome. Cell Rep. *25*, 1525–1536.e7. https://doi.org/10.1016/j.celrep.2018.09.071.

68. Madorin, W.S., Rui, T., Sugimoto, N., Handa, O., Cepinskas, G., and Kvietys, P.R. (2004). Cardiac myocytes activated by septic plasma promote neutrophil transendothelial migration: role of platelet-activating factor and the chemokines LIX and KC. Circ. Res. *94*, 944–951. https://doi.org/10.1161/01.RES.0000124395.20249.AE.

69. Tang, J., Tu, S., Lin, G., Guo, H., Yan, C., Liu, Q., Huang, L., Tang, N., Xiao, Y., Pope, R.M., et al. (2020). Sequential ubiquitination of NLRP3 by RNF125 and Cbl-b limits inflammasome activation and endotoxemia. J. Exp. Med. *217*, e20182091. https://doi.org/10.1084/jem.20182091.

70. Rodríguez-Nuevo, A., Torres-Sanchez, A., Duran, J.M., De Guirior, C., Martínez-Zamora, M.A., and Böke, E. (2022). Oocytes maintain ROS-free mitochondrial metabolism by suppressing complex I. Nature *607*, 756–761. https://doi.org/10.1038/s41586-022-04979-5.

71. Vaux, E.C., Metzen, E., Yeates, K.M., and Ratcliffe, P.J. (2001). Regulation of hypoxia-inducible factor is preserved in the absence of a functioning mitochondrial respiratory chain. Blood *98*, 296–302. https://doi.org/10.1182/blood.v98.2.296.

72. Ge, Y., Zhang, R., Feng, Y., and Li, H. (2020). Mbd2 Mediates Retinal Cell Apoptosis by Targeting the lncRNA Mbd2-AL1/miR-188-3p/Traf3 Axis in Ischemia/Reperfusion Injury. Mol. Ther. Nucleic Acids *19*, 1250–1265. https://doi.org/10.1016/j.omtn.2020.01.011.

73. Sone, M., Morone, N., Nakamura, T., Tanaka, A., Okita, K., Woltjen, K., Nakagawa, M., Heuser, J.E., Yamada, Y., Yamanaka, S., and Yamamoto, T. (2017). Hybrid Cellular Metabolism Coordinated by Zic3 and Esrrb Synergistically Enhances Induction of Naive Pluripotency. Cell Metab. *25*, 1103–1117.e6. https://doi.org/10.1016/j.cmet.2017.04.017.

74. Liu, J., Li, W., Deng, K.Q., Tian, S., Liu, H., Shi, H., Fang, Q., Liu, Z., Chen, Z., Tian, T., et al. (2022). The E3 Ligase TRIM16 Is a Key Suppressor of Pathological Cardiac Hypertrophy. Circ. Res. *130*, 1586–1600. https://doi.org/10.1161/CIRCRESAHA.121.318866.

75. Wang, S., Wang, L., Qin, X., Turdi, S., Sun, D., Culver, B., Reiter, R.J., Wang, X., Zhou, H., and Ren, J. (2020). ALDH2 contributes to melatonin-induced protection against APP/PS1 mutation-prompted cardiac anomalies through cGAS-STING-TBK1-mediated regulation of mitophagy. Signal Transduct. Target. Ther. *5*, 119. https://doi.org/10.1038/s41392-020-0171-5.

76. Zheng, J., Chen, L., Lu, T., Zhang, Y., Sui, X., Li, Y., Huang, X., He, L., Cai, J., Zhou, C., et al. (2020). MSCs ameliorate hepatocellular apoptosis mediated by PINK1-dependent mitophagy in liver ischemia/reperfusion injury through AMPKα activation. Cell Death Dis. *11*, 256. https://doi.org/10.1038/s41419-020-2424-1.

77. Xue, F., Cheng, J., Liu, Y., Cheng, C., Zhang, M., Sui, W., Chen, W., Hao, P., Zhang, Y., and Zhang, C. (2022). Cardiomyocyte-specific knockout of ADAM17 ameliorates left ventricular remodeling and function in diabetic cardiomyopathy of mice. Signal Transduct. Target. Ther. *7*, 259. https://doi.org/10.1038/s41392-022-01054-3.

78. Zhong, H., Lu, J., Xia, L., Zhu, M., and Yin, H. (2014). Formation of electrophilic oxidation products from mitochondrial cardiolipin in vitro and in vivo in the context of apoptosis and atherosclerosis. Redox Biol. *2*, 878–883. https://doi.org/10.1016/j.redox.2014.04.003.

79. Cohen, J. (2000). The detection and interpretation of endotoxaemia. Intensive Care Med. *26*, S51–S56. https://doi.org/10.1007/s001340051119.

80. Shah, N., Dhar, D., El Zahraa Mohammed, F., Habtesion, A., Davies, N.A., Jover-Cobos, M., Macnaughtan, J., Sharma, V., Olde Damink, S.W.M., Mookerjee, R.P., and Jalan, R. (2012). Prevention of acute kidney injury in a rodent model of cirrhosis following selective gut decontamination is associated with reduced renal TLR4 expression. J. Hepatol. *56*, 1047–1053. https://doi.org/10.1016/j.jhep.2011.11.024.

81. Li, B., Yu, M., Pan, X., Ren, C., Peng, W., Li, X., Jiang, W., Zheng, J., and Zhou, H. (2014). Artesunate reduces serum lipopolysaccharide in cecal ligation/puncture mice via enhanced LPS internalization by macrophages through increased mRNA expression of scavenger receptors. Int. J. Mol. Sci. *15*, 1143–1161. https://doi.org/10.3390/ijms15011143.

82. Shi, H., Murray, A., and Beutler, B. (2016). Reconstruction of the Mouse Inflammasome System in HEK293T Cells. Bio. Protoc. *6*, e1986. https://doi.org/10.21769/BioProtoc.1986.

83. Zhang, X., Zuo, X., Yang, B., Li, Z., Xue, Y., Zhou, Y., Huang, J., Zhao, X., Zhou, J., Yan, Y., et al. (2014). MicroRNA directly enhances mitochondrial translation during muscle differentiation. Cell *158*, 607–619. https://doi.org/10.1016/j.cell.2014.05.047.

84. Wittig, I., Braun, H.P., and Schägger, H. (2006). Blue native PAGE. Nat. Protoc. *1*, 418–428. https://doi.org/10.1038/nprot.2006.62.

85. Chin, H.S., Li, M.X., Tan, I.K.L., Ninnis, R.L., Reljic, B., Scicluna, K., Dagley, L.F., Sandow, J.J., Kelly, G.L., Samson, A.L., et al. (2018). VDAC2 enables BAX to mediate apoptosis and limit tumor development. Nat. Commun. *9*, 4976. https://doi.org/10.1038/s41467-018-07309-4.

86. Ma, S.B., Nguyen, T.N., Tan, I., Ninnis, R., Iyer, S., Stroud, D.A., Menard, M., Kluck, R.M., Ryan, M.T., and Dewson, G. (2014). Bax targets mitochondria by distinct mechanisms before or during apoptotic cell death: a requirement for VDAC2 or Bak for efficient Bax apoptotic function. Cell Death Differ. *21*, 1925–1935. https://doi.org/10.1038/cdd.2014.119.

STAR★METHODS

KEY RESOURCES TABLE

REAGENT or RESOURCE	SOURCE	IDENTIFIER
Antibodies		
Mouse monoclonal anti-GSDMDC1 (H-11)	Santa Cruz Biotechnology	Cat#:sc-393581; RRID:AB_2819179
Recombinant rabbit monoclonal anti-LAMP-1 [EPR21026]	Abcam	Cat# ab208943; RRID:AB_2923327
Recombinant rabbit monoclonal anti-PMP70 [EPR5614]	Abcam	Cat# ab109448; RRID:AB_10863068
Recombinant rabbit polyclonal anti-GOLPH3 [EPR21026]	Abcam	Cat# ab98023; RRID:AB_10860828
Recombinant rabbit monoclonal anti-pro Caspase-1 + p10 + p12 [EPR16883]	Abcam	Cat#:ab179515; RRID:AB_2884954
Rat monoclonal anti-Caspase 11	Sigma	Cat#:C1354; RRID:AB_258736
Mouse monoclonal anti-Caspase 4 (clone 4B9)	MBL International	Cat#:M029-3; RRID:AB_590743
Recombinant rabbit monoclonal anti-NLRP3 [EPR23094-1]	Abcam	Cat#:ab263899; RRID:AB_2889890
Rabbit monoclonal anti-HA [EPR22819-101]	Abcam	Cat# ab236632; RRID:AB_2864361
Mouse monoclonal anti-BAX (B-9)	Santa Cruz Biotechnology	Cat#:sc-7480; RRID:AB_626729
Mouse monoclonal anti-BAK (AT38E2)	Santa Cruz Biotechnology	Cat#:sc-517390
Rabbit monoclonal anti-VDAC1/Porin [EPR10852(B)]	Abcam	Cat#:ab154856; RRID:AB_2687466
Mouse monoclonal anti-VDAC2 Antibody	Proteintech	Cat# 66388-1-Ig; RRID:AB_2881764
Rabbit polyclonal anti-VDAC3 Antibody	Proteintech	Cat# 55260-1-AP; AB_10973676
Mouse recombinant anti-MLKL Antibody (E7V4W)	Cell Signaling Technology	Cat#:26539
Rabbit recombinant anti-CASP3 Antibody[EPR18297]	Abcam	Cat#:ab184787; RRID:AB_2827742
Mouse monoclonal anti-CASP8 Antibody(1C12)	Cell Signaling Technology	Cat#:9746; RRID:AB_2275120
Mouse monoclonal anti-CASP8 Antibody(D-8)	Santa Cruz Biotechnology	Cat# sc-5263; RRID:AB_673488
Mouse monoclonal anti-CASP9 Antibody (C9)	Cell Signaling Technology	Cat# 9508; RRID:AB_2068620
Rabbit monoclonal anti-cleaved PARP1 Antibody[E51]	Abcam	Cat# ab32064; RRID:AB_777102
Rabbit polyclonal anti-Rabbit GAPDH	Proteintech	Cat#:10494-1-AP; RRID:AB_2263076
Rabbit polyclonal anti-Rabbit COXIV	Proteintech	Cat#:11242-1-AP; RRID:AB_2085278
normal mouse IgG	Santa Cruz Biotechnology	Cat#:sc-2025; RRID:AB_737182
Rabbit polyclonal anti-Na, K-ATPase	Cell Signaling Technology	Cat#:3010; RRID:AB_2060983
Mouse monoclonal SDHA	Proteintech	Cat#:66588-1-Ig
Mouse monoclonal anti-ubiquitin Antibody (P4D1)	Santa Cruz Biotechnology	Cat# sc-8017; RRID:AB_628423
Rabbit IgG, monoclonal [EPR25A] Antibody	Abcam	Cat# ab172730; RRID:AB_2687931
HRP-conjugated Affinipure Goat Anti-Mouse IgG(H + L)	Proteintech	Cat#:SA00001-1; RRID:AB_2722565
HRP-conjugated Affinipure Goat Anti-Rabbit IgG(H + L)	Proteintech	Cat#:SA00001-2; RRID:AB_2722564
HRP-conjugated Affinipure Goat Anti-Rat IgG(H + L)	Proteintech	Cat#:SA00001-15; RRID:AB_2864369
Recombinant rabbit monoclonal anti-cleaved N-terminal GSDMD [EPR20829-408]	Abcam	Cat#:ab215203; RRID:AB_2916166
Rabbit polyclonal anti-Sarcomeric Alpha Actinin	Abcam	Cat#:ab137346; RRID:AB_2909405
Rabbit monoclonal anti-TOMM20 [EPR15581] - Mitochondrial Marker	Abcam	Cat#:ab186734; RRID:AB_2716623
Goat Anti-Rabbit IgG(H + L), FITC conjugate	Proteintech	Cat#:SA00003-2; RRID:AB_2890897
Alexa Fluor 594-conjugated Goat Anti-Rabbit IgG(H + L)	Proteintech	Cat#:SA00006-4; RRID:AB_2756337
CoraLite 488-conjugated Goat Anti-Mouse IgG(H + L)	Proteintech	Cat#:SA00013-1; RRID:AB_2810983
Chemicals, peptides, and recombinant proteins		
LPS (Escherichia coli O128:B12)	Sigma	Cat#:L2887
LPS-EB Ultrapure	Invitrogen	Cat#:tlrl-3pelps
Poly(I:C)	Invitrogen	Cat#:tlrl-pic
Lipofectamine 2000	Thermo Fisher Scientific	Cat#:11668019

(Continued on next page)

Continued

REAGENT or RESOURCE	SOURCE	IDENTIFIER
Fetal bovine serum	Gibco	Cat#:SH30084.03
Dulbecco's modified Eagle's medium	Gibco	Cat#:SH30022.01
0.25% Trypsin	Gibco	Cat#:25200056
Penicillin-streptomycin solution	KeyGEN BioTECH	Cat#:KGY0023
DAPI	Roche Penzberg	Cat#:23627
Propidium Iodide (PI)	Invitrogen	Cat#:P3566
Triton X-100	Sigma	Cat#:T8787
Bovine serum albumin (BSA)	Sigma	Cat#:A3912
MitoTempol	ENZO Life Science	Cat#:ALX-430-150-M005
XJB-5-131	Sigma	Cat#:866404-31-1
SS-31	ChinaPeptides	Cat#:r-200, 600-DEN-KF-NH2
Dimethyl itaconate	Sigma	Cat#:592498
Dimethyl malonate	Sigma	Cat#:592498
Phosphate-buffered saline	HyClone	Cat#:SH30022.01
SDS lysis buffer	Beyotime Biotechnology	Cat#:P0013G
Protease inhibitor	Cowin Biotech	Cat#:CW2200S
Phosphatase inhibitor	Cowin Biotech	Cat#:CW2383S
TRIzol reagent	Invitrogen	Cat#:15596026
SYBR Green PCR Master Mix	Roche, Basel	Cat#:04913850001
Lipofectamine RNAfit	Hanbio	Cat#:HB-RF-1000
4%–16% acrylamide gradient gels	Thermo Fisher Scientific	Cat#:BN1004BOX
Protein A/G PLUS-Agarose	Santa Cruz Biotechnology	Cat#:sc-2003
Hank's balanced salt solution with calcium and magnesium (HBSS/Ca/Mg)	Gibco	Cat#:14025-092
Rotenone	Sigma	Cat#:R8875
Antimycin A	Abcam	Cat#:ab147494
Oligomycin	Abcam	Cat#:ab141829
1× protease inhibitor	Cowin Biotech	Cat#:CW2200S
1× phosphatase inhibitor	Cowin Biotech	Cat#:CW2383S
RIPA buffer	Beyotime	Cat#:P0013D
Imidazole	Sigma	Cat#:I0250
Tricine	Macklin	Cat#:T818489
Coomassie Blue G-250	Beyotime	Cat#:ST1119
Glutaraldehyde	Karnovsky	Cat#:PH1831
FITC-conjugated LPS (O111:B4)	Sigma	Cat#:F3665
Nigericin	Invivogen	Cat#:tlrl-nig-5
N-acetylcysteine (NAC)	Sigma	Cat#:A9165
ABT-737	MedChemExpress	Cat#:HY-50907
Cardiolipin Mix I	Avanti Polar lipids	Cat#:LM6003
MG-132	Sigma	Cat#:474790-1MG
Chloroquine	MedChemExpress	Cat#:HY-17589A
Critical commercial assays		
MGIEasy RNA Library Prep Kit V3.0 (96 RXN)	MGI	Cat#:1000005272
Mitochondria isolation kit for tissue	Abcam	Cat#:ab110168
Membrane protein extraction kit	Thermo Fisher Scientific	Cat#:89842
Mitochondria Isolation Kit for Cultured Cells	Thermo Fisher Scientific	Cat#:89874
Bicinchoninic acid assay (BCA)	KeyGEN BioTECH	Cat#:KGP903
NativePAGE Sample Prep Kit	Thermo Fisher Scientific	Cat#:BN2008
Lactate Dehydrogenase (LDH) Release Assay Kit	Beyotime	Cat#:C0017

Continued

REAGENT or RESOURCE	SOURCE	IDENTIFIER
Annexin V-FITC kit	BD Biosciences	Cat#:556547
MitoSOX Red mitochondrial superoxide indicator	Thermo Fisher Scientific	Cat#:M3600
dihydroethidium (DHE)	Sigma	Cat#:D7008
In Situ Cell Death Detection Kit, TMR red	Roche Applied Science	Cat#:12156792910
ATP assay kit	Beyotime	Cat#:S0026B
Reverse Transcription Reagent Kit	Transgene	Cat#:205410
Deposited data		
Bulk RNA sequencing: Raw and analyzed data	This paper	GSE215131
Code for bulk RNA sequencing and analysis	This paper	https://github.com/JJClab/heart.git
Experimental models: Cell lines		
Human: AC16 Human Cardiomyocyte Cell Line	Sigma	Cat#:SCC109; RRID:CVCL_4U18
Human: NLRP3 $^{-/-}$ AC16 cells	Cyagen Biosciences	Cat#:STSKO230828CXW1
Human: HEK293T	American Type Culture Collection (ATCC)	Cat#:CRL-3216; RRID:CVCL_0063
Experimental models: Organisms/strains		
Mouse: C57BL/6J	Hunan Slac Jingda Laboratory	SCXK2016-0002
Mouse: *Casp11*$^{-/-}$	Timothy R. Billiar Lab; Tang X et al., 2021[44]	N/A
Mouse: *Gsdmd*$^{-/-}$	Timothy R. Billiar Lab; Yang et al.[43]	N/A
Mouse: *Tlr4*$^{-/-}$	Timothy R. Billiar Lab; Tang et al.[44]	N/A
Mouse: *Casp1*$^{-/-}$	Timothy R. Billiar Lab; Xu et al.[45]	N/A
Mouse: *Nlrp3*$^{-/-}$	Lu Lab; Tang et al.[44]	N/A
Mouse: B6/JGpt-*Gsdmd*^{em1Cflox}/Gpt (*Gsdmd*$^{fl/fl}$)	GemPharmatech	RRID:IMSR_GPT:T008770
Mouse: *Myosin heavy chain 6*-Cre (*Myh6*-Cre)	Jackson Laboratory	JAX: C001041
Oligonucleotides		
siRNA targeting sequence: *TLR4* Human: TGGTGAGTGTGACTATTGA	Ribobio	#stB0000947B
siRNA targeting sequence: *NLRP3* Human: CCTCGGTACTCAGCACTAATT	Hanbio	#HH20210118HNSLY-SI03
siRNA targeting sequence: *CASP4* Human: GCCUCAGUCUGAAGGACAATT	Hanbio	#HH20210118HNSLY-SI02
siRNA targeting sequence: *CASP1* Human: GCACACGUCUUGCUCUCAUTT	Hanbio	#HH20210118HNSLY-SI01
siRNA targeting sequence: *GSDMD* Human: GCAGGAGCUUCCACUUCUATT	Hanbio	#HH20210628HNSLY-SI01
siRNA targeting sequence: *CLS* Human: GAUGCACCACAUCUAGUAATT	Hanbio	#HH20201214HNSLY-SI01
siRNA targeting sequence: *PLS3* Human: GACAUGUUAUACCAAUGAATT	Tsingke	#C203299825
siRNA targeting sequence: *GAPDH* Human: GUGGAUAUUGUUGCCAUCATT	Tsingke	#C203299829
siRNA targeting sequence: *BAX* Human: GACGAACUGGACAGUAACAUG	Hanbio	#HH20230215HNSLY-SI01
siRNA targeting sequence: *BAK* Human: GCTTCGTGGTCGACTTCAT	Ribobio	#stB0003728C
siRNA targeting sequence: *VDAC1* Human: ACACTAGGCACCGAGATTA	Ribobio	#siB11825153448
Primers for *TLR4, NLRP3, CASP4,CASP1,GSDMD, CLS, PLS3, BAX, BAK, VDAC1,* Human, see Table S5 for a list of oligonucleotides	This paper	N/A

(Continued on next page)

Continued

REAGENT or RESOURCE	SOURCE	IDENTIFIER
Recombinant DNA		
Plasmid: pcDNA3.1 h-FL-GSDMD	This paper	N/A
Plasmid: pcDNA3.1 h-NT-GSDMD	Hanbio	Addgene Plasmid: #HH20200828HNSLY-PC01
Plasmid:pcDNA3.1 h-NT-GSDMD (E15K)	This paper	N/A
Plasmid:pcDNA3.1 h-NT-GSDMD (L192D)	This paper	N/A
Plasmid:pcDNA3.1 h-NT-GSDMD (E15K/L192D)	This paper	N/A
Plasmid: pcDNA3.1 h-IL-1b-myc	Hanbio	Addgene Plasmid: #HH20230902HNSLY-PC01
Plasmid: pcDNA3.1 h-CASP-1-HA	Hanbio	Addgene Plasmid: #HH20230902HNSLY-PC01
Plasmid: pcDNA3.1 h-GFP-PYCARD	Hanbio	Addgene Plasmid: #HH20230902HNSLY-PC01
Plasmid: pcDNA3.1 h-NLRP3-3FLAG	Hanbio	Addgene Plasmid: #HH20230902HNSLY-PC01
Software and algorithms		
FlowJo software version 7.6	TreeStar	https://www.flowjo.com/
Image Lab 3.0 software	Bio-Rad	https://www.bio-rad.com/zh-cn/product/image-lab-software?ID=KRE6P5E8Z
ImageJ software	National Institutes of Health	https://oit.utk.edu/research/research-software/imagej/
Adobe Illustrator 2020	Adobe	https://www.adobe.com/
ZEN 2 (blue edition)	Carl Zeiss	https://www.micro-shop.zeiss.com/en/de/
Prism 8	Graph Pad	https://www.graphpad-prism.cn/
R version 4.2.1	The R Foundation	https://cran.r-project.org/bin/windows/base/
Compound Discoverer Software version 3.3	Thermo Fisher Scientific	https://www.thermofisher.cn/cn/zh/home/products-and-services/promotions/industrial/compound-discoverer.html

RESOURCE AVAILABILITY

Lead contact
Requests for additional information, resources, and reagents should be directed to the lead contact, Jingjing Cai (caijingjing83@hotmail.com; caijingjing@csu.edu.cn).

Materials availability
This study did not generate new unique reagents.

Data and code availability
Bulk RNA-seq data have been deposited at GEO and are publicly available as of the date of publication. Accession numbers are listed in the key resources table. All original code has been deposited on Github and is publicly available as of the date of publication. The DOI is listed in the key resources table. Original western blot images and microscopy data reported in this paper will be deposited at Mendeley before the date of publication and shared by the lead contact upon request. Any additional information required to reanalyze the data reported in this paper is available from the lead contact upon request.

EXPERIMENTAL MODEL AND STUDY PARTICIPANT DETAILS

Mouse studies
Male C57BL/6J mice (8–10 weeks old) were purchased from Hunan Slac Jingda Laboratory Animal Company, Ltd. (Certificate SCXK2016-0002). *Tlr4*$^{-/-}$ mice, *Gsdmd*$^{-/-}$ mice, *Casp1*$^{-/-}$ mice, and *Casp11*$^{-/-}$ mice were provided by Professor Timothy R. Billiar

at the University of Pittsburgh Medical Center.[53–55] $Nlrp3^{-/-}$ mice were provided by Professor Ben Lu at Central South University.[54] WT male C57BL/6J mice were used as controls for the above-mentioned transgenic mice. B6/JGpt-$Gsdmd^{em1Cflox}$/Gpt ($Gsdmd^{fl/fl}$) mice were generated by CRISPR/Cas9-mediated genome editing from the GemPharmatech Co. Ltd (RRID: IMSR_GPT: T008770). *Myh6-Cre* transgenic mice were purchased from Jackson Laboratory (JAX: 011038). Cardiomyocyte-specific knockout ($Gsdmd^{fl/fl}$; Myh6-Cre [*Gsdmd-CKO*]) mice were generated by crossing $Gsdmd^{fl/fl}$ mice with the *Myh6-Cre* strain from Cyagen Biosciences Inc. Littermates not carrying the *Myh6-Cre* transgene ($Gsdmd^{fl/fl}$) were used as controls. $Tlr4^{-/-}$ mice, $Gsdmd^{-/-}$ mice, $Casp1^{-/-}$ mice, and $Casp11^{-/-}$ mice were maintained on a 12-h light-dark cycle in a pathogen-free facility at the University of Pittsburgh (Pittsburgh, PA, USA). $Nlrp3^{-/-}$ mice, $Gsdmd^{fl/fl}$ mice, and *Gsdmd-CKO* mice were maintained on a 12-h light-dark cycle, 22°C–24°C room temperature, and 40%–70% humidity in a pathogen-free facility at Central South University (Changsha, Hunan, China). All transgenic strains were backcrossed at least 10 times into a C57BL/6J background and used at the age of 8–10 weeks. All animal experiments and protocols were approved by the Animal Care and Use Committee and the Ethics Committee of Central South University or the University of Pittsburgh. The sample size was determined by power calculations with an α level of 0.05 and power of 0.80, at least 6 mice per group were required. To reduce variability and avoid the interference of estrogen and the menstrual cycle, only male mice were used in the study. Randomization and allocation concealment were performed. All transgenic mice used in our research were confirmed using standard genotyping techniques. The primers used for genotyping transgenic mice are available in Table S5. Echocardiography assessment in any groups revealed no significant differences in heart rate (Tables S1, S2, and S4).

Endotoxin-induced myocardial dysfunction *in vivo*

A murine model of endotoxemia was constructed according to a previous study from our group.[22–24] All mice were injected intraperitoneally (i.p.) for priming with 1 mg/kg Poly(I:C) (tlrl-pic, Invitrogen, California, USA) and 7 h later treated with LPS (10 mg/kg, i.p.) (*Escherichia coli* O128:B12, L2887, Sigma, St. Louis, MO, USA) dissolved in 0.9% sterile sodium chloride for 4 h or 14 h.

Animal treatments and reagents

To reduce mitochondrial-generated oxidants, 10, 15, 20 mg/kg MitoTempol (ALX-430-150-M005, ENZO Life Science, Farmingdale, NY, USA) dissolved in 0.9% sterile sodium chloride was injected i.p. 1 h before Poly(I:C) and LPS challenge.[56]

To selectively inhibit CL oxidation, 10 mg/kg XJB-5-131 (866404-31-1, Sigma, St. Louis, MO, USA) dissolved in sterile phosphate-buffered saline (PBS) was pretreated i.p. 1 h before Poly(I:C) and LPS exposure, while 5 mg/kg SS-31 (r-200, 600-DEN-KF-NH2, ChinaPeptides, Shanghai, China) in PBS was injected twice at 30 min before Poly(I:C) and 30 min before LPS stimulation due to its poor specific biodistribution and low delivery efficiency.[57,58]

For complex II inhibition, DI (0.69 mg/g) (592498, Sigma, St. Louis, MO, USA) or DMM (160 mg/kg) (136441, Sigma, St. Louis, MO, USA) in PBS was administered i.p. 10 min before Poly(I:C) and LPS challenge.[31,59,60]

Cell lines culture

The AC16 cell line was purchased from the Sigma-Aldrich Company (Cat#SCC109, RRID: CVCL_4U18, Sigma, St. Louis, MO, USA) and the HEK293T cell line was obtained from the American Type Culture Collection (Cat#CRL-3216, RRID: CVCL_0063, ATCC, Manassas, Virginia, United States). The two cell lines were generated from female donors and then immortalized with SV40. The cells were cultured in Dulbecco's modified Eagle's medium (DMEM) (SH30022.01, Gibco, Grand Island, NY, USA) containing 10% fetal bovine serum (FBS) (SH30084.03, Gibco, Grand Island, NY, USA) and 1% penicillin-streptomycin solution (KGY0023, KeyGEN BioTECH, Nanjing, Jiangsu, China) in a humidified incubator at 37°C and 5% CO_2.

Culture of primary neonatal rat cardiomyocytes (NRCMs)

Briefly, NRCMs were isolated and cultured as described in our previous studies.[61,62] Male Sprague–Dawley rats at 1 to 3 days old were euthanized by cervical dislocation. The heart tissues were immediately dissected in a sterile environment, and residual blood was washed away with PBS. The ventricular tissue was separated from the atria and was trisected and digested repeatedly with 0.25% trypsin (25200056, Gibco, Grand Island, NY, USA) at 37°C for 5 min per cycle. After 7–10 cycles, the obtained cells were cultured at 37°C in a humidified 5% CO_2 incubator. Three hours later, the supernatant containing suspended cardiomyocytes was transferred into another dish with DMEM containing 10% FBS for 48 h and then replaced with a fresh medium.

CRISPR/Cas9-mediated generation of NLRP3$^{-/-}$ AC16 cells

CRISPR/Cas9 genomic editing for gene deletion was performed according to the previous publication.[63] Guide RNA sequences targeting NLRP3 (5′- TTAGCGTGGCTAGATCCACA-3′) with BsmbI sticky end were selected for their position and a low number of predicted off-targets. The off-target analysis is based on the GRCh38/hg38 assembly (2013). PCR sequencing was required to screen positive colonies of the frameshift mutation, when sgRNA was designed to construct Cas9 and sgRNA plasmids, followed by target cell line (AC16, NCBI Taxonomy: 9606) transfection via electroporation. AC16 cells were tested for bacteria, mold, mycoplasma and other contaminants. Clonal efficiency was measured to determine cell proliferation. The region containing the mutation was sequenced to confirm the genotype. Stable transduced cells were isolated from single clones and enriched for screening. Colonies were genotyped by PCR and sequencing to validate successful knockout. Clones were identified by immunoblotting with anti-NLRP3 antibodies, and the NLRP3$^{-/-}$ clone was used for the indicated analyses. Positive clones will be Cryopreserved.

Endotoxin-induced cardiomyocyte injury *in vitro*

AC16 cells and primary NRCMs were primed with or without 1 μg/mL Poly(I:C) for 3 h and transfected with various doses of LPS (10, 100, 10000 ng/mL)(TLRL-3PELPS, Invitrogen, California, USA) using 6 μL/mL Lipofectamine 2000 (11668019, Thermo Fisher Scientific, California, USA) according to the manufacturer's protocol.

Cell treatments and reagents

For mitochondrial-targeted antioxidants, cells were pretreated with 25, 250, and 2500 nM MitoTempol 1 h before 1 μg/mL Poly(I:C) priming and subsequent 10 ng/mL LPS stimulation.[64]

For selective CL oxidation inhibitors, XJB-5-131 or SS-31 was added immediately to fresh DMEM before 1 μg/mL Poly(I:C) priming to achieve a final concentration of 10 μM.[44,65]

To directly induce oxidative stress, cells were treated with H_2O_2 (100 mM) for 1 h[66]

To activate the NLRP3 inflammasome, 10 ng/mL LPS primed for 2 h and followed by 5 μM nigericin (Sigma-Aldrich) for 1 h[67]

To determine whether NLRP3 undergoes proteasome or lysosome-mediated degradation, AC16 cells were pretreated with MG-132 (5 μM) or Chloroquine (10 μM) for 30 min, and then with Poly(I:C) priming + LPS stimulation or LPS priming + nigericin stimulation.[35,68,69]

In the inhibitory studies, cells were pretreated with N-acetylcysteine (NAC, 25 mM) (Sigma-Aldrich) or extracellular potassium chloride (100 mM) 30 min before challenge with 1 μg/mL Poly(I:C).[67]

To activate BAX/BAK oligomer and apoptosis, ABT-737 (100 nM), a BH3 mimic, was applied to cells for 7 h[29,30]

To determine the source of mROS in cardiomyocytes during endotoxemia, the complex I inhibitor rotenone (0.1 μM)(R8875, Sigma, St. Louis, MO, USA), the complex II inhibitors DMM (10 mM) or DI (250 μM), the complex III inhibitor antimycin A (4 μM) (ab147494, Abcam, Cambridge, MA, USA), the complex IV inhibitor KCN (50 mM)(1049670100, Millipore, Merck KGaA, Darmstadt, Germany), and ATP syntheses inhibitor oligomycin (10 μM) (ab141829, Abcam, Cambridge, MA, USA) were added 3 h before Poly(I:C) priming +10 ng/mL LPS stimulation.[31,59,60,70–73]

Cells were pretreated with an equal volume of DMEM as controls. All results were normalized to those of the control group.

METHOD DETAILS

Echocardiography

Echocardiography was performed to evaluate the cardiac function at the specified time point after endotoxin challenge in various strains. Small animal echocardiography (Vevo 2100, FUJIFILM VisualSonics, Inc., Toronto, Canada) equipped with a 30 MHz linear transducer was used for the measurements. M-mode images were taken in planes that approximated the parasternal short-axis and apical long-axis.[74,75] The left ventricle and the aortic outflow tract were observed in a two-dimensional B-mode, and the sample line was placed at the maximum cross-section of the left ventricle to guide the recording of serial M-mode echocardiographic images. The left ventricular internal diameter at end-diastole (LVIDd) and left ventricular internal diameter at end-systole (LVIDs) were measured at the mid-papillary muscle level. The left ventricular end-diastolic volume (LVEDV) and left ventricular end-systolic volume (LVESV) were measured according to the maximum and minimum left ventricular area. LVEF was calculated as LVEF=(LVEDV-LVESV)/LVEDV×100%. LVFS was calculated as LVFS=(LVIDd-LVIDs)/LVIDd×100%. The LVAWd, LVPWd, and LVIDd were measured to estimate the LV mass (mg) = 1.053 x [(LVAWd+LVPWd+LVIDd)^3-LVIDd^3]. All parameters were measured for five separate cardiac cycles per mouse.

Cardiac tissue harvest and preparation

For bulk RNA sequencing and real-time quantitative polymerase chain reaction, mice were perfused with cold PBS through the ascending aorta, and their heart tissues were dissected, harvested in TRIzol reagent (15596026, Invitrogen, Carlsbad, CA, USA), and stored at −80°C for further analysis.

For mitochondrial isolation, the myocardium was separated and stored at −80°C until use.

For DHE staining, Mitosox staining, and immunostaining, the fresh left ventricular tissues were directly embedded in an optimum cutting temperature compound without fixation and stored at −80°C.

For terminal deoxynucleotidyl transferase-mediated dUTP-biotin nick-end labeling (TUNEL) and immunofluorescence staining, the cardiac apex was cut, fixed in 4% paraformaldehyde overnight, dehydrated in 30% sucrose for 24 h, embedded in optimum cutting temperature compound, and transferred to −80°C for storage.

For transmission electron microscope, the heart samples were cut into 1-mm^3 pieces, fixed with 2.5% glutaraldehyde (PH1831, Karnovsky, Beijing, China) in 0.1 M phosphate buffer at 4°C for 1 h, dehydrated, and stored at 4°C.

Bulk RNA sequencing

Total RNA was extracted from heart tissue as described in our recent study.[24] The RNA quality and quantity were tested with 1% agarose gels, a NanoDrop, and an Agilent 2100 bioanalyzer (Thermo Fisher Scientific, MA, USA). cDNA libraries were constructed using an MGIEasy RNA Library Prep Kit V3.0 (96 RXN) (1000005272, MGI, Shenzhen, China) and RNA sequencing was performed on a BGISEQ-500 platform according to the manufacturer's instructions (BGI, Guangdong, China). After removing reads with low

quality with FastQC, the clean reads were aligned to a mouse genome (mm10) with HiSat2 (version 2.0.4) and Bowtie2 (version 2.2.5), sorted with RSEM (version 1.2.12), and assembled with StringTie (version 1.3.3.13); scater was used for quality control. The count information was further taken as the input of DESeq2 (version 1.4.5) for differentially expressed genes (DEGs) identified with adjusted p value less than 0.05 and $\log_2$[fold change] > 1.5. After log-normalizing the data, Principal component analysis was performed for dimension reduction. Heatmaps and volcano plots of the DEGs were plotted with the R package ggplot2 (version 3.3.5). GSEA (version 4.0.1) software was used in the LPS 4-h group compared to the Poly 7-h group and control group, respectively. A curated gene set (C2 term) was obtained from the molecular signatures database. Pathway sets with a p-value of <0.05 and a false discovery rate value of <0.25 were considered statistically significant. The top10 significantly upregulated signaling pathways were screened out based on the normalized enrichment score in each pathway through the ggplot2 package in R.

Preparation of tissue subcellular fractions

Mitochondrial fractions were isolated by using a mitochondria isolation kit for tissue (ab110168, Abcam, Cambridge, MA, USA) according to the manufacturer's instructions. Briefly, the heart tissues were suspended, washed, and minced in 1.5 mL of cold wash buffer. The tissues were homogenized in 2.0 mL of isolation buffer with thirty-five strokes in a prechilled Dounce homogenizer (YA0856, Solarbio, Beijing, China), and then was centrifuged at 1,000 ×g for 10 min at 4°C to remove unbroken cells. The supernatant with 2.0 mL of isolation buffer was subsequently centrifuged at 12,000 × g for 15 min at 4°C to collect the pellet. The final supernatant (cytosolic fraction) was transferred to new tubes and stored at −80°C. The pellet containing mitochondria was washed twice by resuspension in 1.0 mL of isolation buffer supplemented with 10 μL of protease inhibitor cocktail and then centrifuged at 12,000 × g for 15 min at 4°C for further purification.

The cell membrane fraction was isolated by using a membrane protein extraction kit (89842, Thermo Fisher Scientific, MA, USA) according to the manufacturer's instructions. In brief, the heart tissues were washed, minced, and suspended in 4.0 mL of cell wash solution. Then, the suspension was homogenized via ten strokes with a prechilled Dounce homogenizer in 1.0 mL of permeabilization buffer, transferred to a new tube, and incubated for 10 min at 4°C in an additional 1.0 mL of permeabilization buffer with constant mixing. The homogenate was centrifuged at 16,000 × g for 15 min at 4°C to collect the pellet, which was the cell membrane fraction. Subcellular fractions were characterized using immunoblotting and antibodies against GAPDH (cytosolic), COXIV or SDHA (mitochondrial), Na, K-ATPase (cell membrane), LAMP1 (lysosome), PMP70 (peroxisomes), and GOLPH3 (golgi).[67]

Detection of ROS and mROS production in heart tissues

The level of total ROS production in the heart tissues was determined by DHE staining according to our previous report.[74] Five-micrometer-thick non-fixed fresh frozen heart tissues were incubated with 5 mM DHE (D7008, Sigma, St. Louis, MO, USA) for 30 min in the dark at 37°C. The levels of mROS production in the heart tissues were measured by 5 μM Mitosox red staining (M3600, Invitrogen, California, USA). Five-micrometer-thick non-fixed frozen heart tissues were incubated with Mitosox red in the dark at 37°C for 15 min. The sections were then washed and images were captured using a fluorescence microscope (SpinSR10, Olympus, Tokyo, Japan). Five fields were randomly obtained from each sample, and the DHE-positive or Mitosox red-positive relative fluorescence was analyzed using ImageJ software as previously described by our team.[76] All quantitative results were normalized to those of the control group, and representative images are shown.

TUNEL staining and immunostaining in heart tissue

For histological analysis, fixed frozen heart tissues were serially cryosectioned at a thickness of 5 μm. The cryosections were fixed in 4% paraformaldehyde for 30 min and then rinsed in PBS. The plasma membranes were permeabilized with 0.1% Triton X-100 (T8787, Sigma, St.Louis, USA). Then, the sections were incubated with TUNEL staining by using an *In Situ* Cell Death Detection Kit, TMR red (12156792910, Roche Applied Science, Penzberg, Germany) according to the manufacturer's instructions. Nonspecific binding sites were blocked by 5% bovine serum albumin (BSA) (A3912, Sigma, St. Louis, USA) in PBS for 30 min. The slides were then incubated with a rabbit anti-sarcomeric alpha-actinin primary antibody (Cat#ab137346, [1:200], RRID: AB_2909405, Abcam, Cambridge, USA) overnight at 4°C. Then, the slides were rinsed and incubated with appropriate secondary antibodies at room temperature for 1 h. Subsequently, the nuclei were labeled with DAPI (23627, [1:4000], Roche Penzberg, Germany) for 1–5 min. The stained slides were photographed with a confocal fluorescence microscope (SpinSR10, Olympus, Tokyo, Japan). The percentage of TUNEL$^+$actinin$^+$ double-positive cells was calculated among 100 cells in each of the 5 randomly selected fields in each section according to recent studies.[76,77] The quantitative results were normalized to those of the control group, and representative images are shown.

Quantification of CL and oxCL by UHPLC-HRMS/MS

Approximately 1 mg of mitochondria from heart tissue was used to extract total lipids using a previous method.[78] In brief, 300 μL methanol and 50 μL of 50 times of diluted Cardiolipin Mix I (LM6003, Avanti Polar lipids, St. Louis, MO, USA) as internal standards were added to each isolated mitochondrial sample. The mixture was vortexed for 30s, then 1000 μL methyl *t*-butyl ether with 0.05% Butylated hydroxytoluene was added to extract total lipids by strongly vortex for 1 min. After centrifuging, the supernatant was collected for evaporating to dryness under nitrogen. Then, the bottom phase was re-extracted by 750 μL hexane/isopropanol (3:2, 0.05% Butylated hydroxytoluene). The supernatant was combined to dry under nitrogen. The dried residue was redissolved

in 50 μL methanol, and the supernatant was transferred to the vial for the UHPLC-HRMS/MS analysis of CLs and oxCL on a ThermoFisher Ultimate 3000 UHPLC system with an Acclaim C30 column (2.1 mm × 100 mm, 3 μm, Thermo Fisher Scientific, California, USA) at 50°C. The eluents were analyzed on a ThermoFisher Q Exactive Hybrid Quadrupole Orbitrap Mass Spectrometry in Heated Electrospray Ionization Negative mode. The spray voltage was 3.5 kV. Both Capillary and Aux Gas Temperature were 350°C. The flow rates of Sheath gas and Aux gas were 40 (Arb) and 10 (Arb), respectively. S-Lens RF Level was 50 (Arb). The preprocessing of raw data and structural identification of metabolite were performed using the commercial software Compound Discoverer (version 3.3) by Thermo Fisher Scientific. The main parameters including mass-to-charge ratio (m/z) of parent ion and mass spectra of fragment ions were set as mass tolerance of 10 ppm for all steps, retention time tolerance of 0.1 min for the peak group, and default values for other parameters. Both isotopic and adduct ion peaks were identified and redundant peaks were excluded in the data analysis.

Measurement of intracellular endotoxin levels

Limulus amebocyte lysate (LAL) and chromogenic kinetic assay (EC80545S, Bioendo, Xiamen, China) were used to detect intracellular endotoxin levels. Approximately 2×10^5 cells were centrifuged (800 rpm for 5 min), and the pellet was resuspended in 100 μL endotoxin-free water. Then, 100 μL of sample and 100 μL of LAL reagent were mixed and heat treated for 1 min at 37°C. After incubation, 100 μL of chromogenic matrix solution was added and incubated at 37°C for 2 min. Next, Azo reagent 1, Azo reagent 2, and Azo reagent 3 were added and mixed in sequence and allowed to stand for 5 min. Absorbance was analyzed at 545 nm with a spectrophotometer using the Endoscan-V software (Charles River Laboratories, Charleston, SC, USA). Results are expressed as EU/mL.[79,80]

To observe LPS internalization, AC16 cells were primed with 1 μg/mL Poly(I:C) for 3 h and transfected with 10 ng/mL FITC-conjugated LPS (F8666, O55:B5, 1 μg/mL, Sigma, St. Louis, MO, USA) for 2 h using 6 μL/mL Lipofectamine 2000 (11668019, Thermo Fisher Scientific, California, USA). After stimulation, Hoechst33342 (1 μg/mL) were added for 10 min to nuclear staining. Then, cells were washed in PBS twice. Images were captured at 1h after stimulation using a confocal laser scanning microscope (Zeiss LSM900+Airyscan 2, Carl Zeiss, Germany). All imaging data are representative of at least three randomly selected fields.[81]

Plasmid transfection

The mutation of leucine192 to aspartate (L192D) or glutamic acid 15 to lysine (E15K), or double mutation in the auto-inhibited region in GSDMD-N was previously described.[12] Plasmids encoding full-length, WT GSDMD-N, E15K-mutant GSDMD-N, L192D-mutant GSDMD-N, and E15K/L192D-mutant GSDMD-N were cloned from cDNAs and ligated to the pcDNA3.1 vector. The constructed plasmid was amplified and confirmed by sequencing. In the transfection experiments, AC16 cells were plated at 2.5×10^5 cells/mL in 15 cm dishes (20 mL/dish), and HEK293T cells were seeded at 6×10^5 cells/mL in 10 cm dishes (10 mL/dish) with DMEM containing 10% FBS without antibiotics for 20 h. On the following day, the AC16 cells were transfected with 20 μg of plasmid DNA in 8.0 mL of Opti-MEM per dish, and HEK293T cells were transfected with 15 μg of plasmid DNA in 6 mL of Opti-MEM per dish using Lipofectamine 2000 (5 μL/mL). The supernatants and cells were collected from 6 to 24 h to test LDH activity and mROS levels to determine the appropriate time points at which exogenous GSDMD-N initiates mitochondrial oxidative stress without cell death for subsequent experiments. All results were normalized to those of the empty vehicle group.

Reconstitution of NLRP3 inflammasome in NLRP3$^{-/-}$ AC16 cells

A standard reconstitution system in HEK293T cells was performed.[82] NLRP3$^{-/-}$ AC16 cells were seeded into 6-well plates at a density of 2×10^4 cells per well in a complete cell culture medium overnight before transfection. The cells were transfected with plasmids expressing pro-IL-1β-myc (1 μg/well), pro-caspase-1-HA (2.5 μg/well), ASC-GFP (100 ng/well), and NLRP3-3*flag (1 μg/well) using Lipofectamine 3000. 36 h–48 h later, replace the medium with DMEM cell culture medium, then the indicated treatments was added.

siRNA transfection

siRNAs targeting human *NLRP3*, *CASP4*, *CASP1*, *GSDMD*, *BAX,* and negative control (*NC*) siRNA were obtained from Hanbio (Shanghai, China). siRNAs targeting *CLS* and *PLS3* were purchased from Tsingke (Beijing, China). siRNAs targeting *TLR4, BAK, and VDAC1* were purchased from Ribobio (Guangzhou, China). For siRNA transient transfections, AC16 cells were seeded in 6-well plates or appropriate dishes in DMEM supplemented with 10% FBS for 20 h and then incubated with 40 nM of the indicated siRNA dissolved in DMEM containing 4 μL/mL of Lipofectamine RNAfit (HB-RF-1000, Hanbio, Shanghai, China) in 2–10 mL of DMEM with 10% FBS per well or dish for 24 h according to the manufacturer's instructions. The silencing efficiency was examined by RT−qPCR at least 24 h later. The siRNA sequences used in this study are listed in the key resources table.

mROS measurement using flow cytometry

mROS were detected in live AC16 and HEK293T cells using the Mitosox red mitochondrial superoxide indicator according to the manufacturer's instructions. Briefly, cells were stained with 5 μM Mitosox red and incubated for 10 min at 37°C protected from light. Then, they were gently washed with warm Hank's balanced salt solution with calcium and magnesium. Mitosox red-positive cell counts were determined by flow cytometry (BD FACSCalibur, USA) and analyzed using FlowJo software version 7.6 (TreeStar Inc., USA). The mean fluorescence intensity was quantified as mROS production. The quantitative results were normalized to those of the control group.

JC-1 staining for mitochondrial membrane potential measurement

Mitochondrial membrane potential was measured by JC-1 staining (T3168, Invitrogen, California, USA). At the indicated time points, AC16 cells were stained with 1 mM JC-1 dye for 30 min at 37°C in the dark and then gently washed twice with 1 × PBS with 4% FBS. The cell fluorescence of 5,000 cells for each sample was measured by flow cytometry and analyzed by Flowjo 7.6. Excitation and emission settings were 488 nm. JC-1 aggregates and monomers were measured under Texas Red (610/20 600LP) and FITC (525/50 505LP), respectively. All quantitative results were normalized to those of the control group.

Apoptosis measurement using Annexin V/PI staining

Apoptotic cells were detected with an Annexin V-FITC kit (556547, BD Biosciences). Cardiomyocytes were stained with 5 μL of Annexin V-FITC for 15 min and 5 μL of Propidium Iodide (PI) (P3566, Invitrogen, California, USA) protected from light. Cardiomyocytes were gently washed with 1 × binding buffer. Annexin V-FITC+PI- and Annexin V-FITC+PI+ staining were confirmed by flow cytometry and analyzed using FlowJo 7.6.

Cytotoxicity assay

Cytotoxicity in AC16 and HEK293T cells was measured with an LDH Release Assay Kit (C0017, Beyotime Biotechnology; Wuhan, China) according to the manufacturer's instructions. Briefly, One hour prior to the time point, 100 μL of LDH releasing reagent was added to the complete cell lysis control wells and incubated. At the indicated time points, the supernatant was collected from each well, centrifuged at 400 × g for 5 min, and then transferred to a 96-well plate. 60 μL of Diluent/Substrate Assay Mix was added to each well and incubated at room temperature in the dark for 30 min. The plate was then analyzed by spectrophotometry at 490 nm, and cell death was calculated as following: cytotoxicity (LDH release (%) = 100 x (experimental LDH release/maximum LDH release). The results were the triplicate mean cell cytotoxicity results.

Confocal microscopy

To detect whether GSDMD-N accumulates in the OMM, AC16 cells were seeded into a 35 mm confocal dish (801001, NEST Biotechnology, Hong Kong, China) and treated with various stimuli. At the indicated time points, AC16 cells were fixed in 4% paraformaldehyde for 15 min, rinsed in PBS, and permeabilized with 0.3% Triton X-100. Nonspecific binding sites were blocked by 3% BSA for 30 min. Subsequently, cells were incubated with rabbit anti-cleaved N-terminal GSDMD (Cat#ab215203, [1:25], RRID: AB_2916166, Abcam, Cambridge, USA) and an antibody for an outer mitochondrial membrane protein (mouse anti-TOMM20, Cat#ab186734, [1:500], RRID: AB_2716623, Abcam, Cambridge, USA) overnight at 4°C and then with appropriate secondary antibodies for 1 h at room temperature. The nuclei were labeled with DAPI. Images were obtained via a confocal laser scanning microscope (Zeiss LSM900+Airyscan 2, Carl Zeiss, Germany). All imaging data are representative of at least three randomly selected fields.

Cellular ATP content

Cellular ATP content was measured by using an ATP assay kit (S0026B, Beyotime Biotechnology, China) according to the manufacturer's instruction. After stimulation, 2×10^5 cells were centrifuged (14,000 g for 10 min), and the supernatant was collected for ATP assay. The luminescence was recorded in an Illuminometer with an integration time of 10 s per well. The cellular ATP content was determined by the chemiluminescence method via a Luminoskan Ascent Serial luminometer (Thermo RS-232C, USA). The results were normalized to the concentration of protein using BCA Protein Assay Kit (KGP903, KeyGEN BioTECH, China).[83]

RNA extraction and RT–qPCR

Total RNA was extracted using TRIzol reagent and quantified using a NanoDrop 2000 (Thermo Fisher Scientific, Waltham, MA, USA). 1 μg of RNA was reverse-transcribed into cDNA with a Reverse Transcription Reagent Kit (205410, Transgene, Illkirch, France). SYBR Green PCR Master Mix (04913850001, Roche, Basel, Switzerland) was used to quantify the PCR products using a CFX 96 Real-Time PCR System (CFX 96 Touch, Bio-Rad, California, USA). *Gapdh* was used as an internal reference. The sequences of the primers used in the current study are listed in Table S5.

Subcellular fractionation

The mitochondrial and cytosolic fractions of cardiomyocytes and HEK293T cells were separated with a Mitochondria Isolation Kit for Cultured Cells according to the manufacturer's instructions (89874, Thermo Fisher Scientific, Waltham, MA, USA). Briefly, approximately 1×10^7 cells were centrifuged (800 rpm for 5 min), and the pellet was resuspended in 800 μL of Mitochondria Isolation Reagent A, vortexed at medium speed for 5 s, and incubated on ice for 2 min. The swollen cells were then homogenized using a prechilled Dounce homogenizer with 46 strokes. The minced cells were added to a mixture of 800 μL of Mitochondria Isolation Reagent C and 200 μL of Mitochondria Isolation Reagent A. The nuclei were separated by centrifugation at 700 × g for 10 min at 4°C. The supernatants were transferred to a new set of tubes and centrifuged again at 12,000 × g for 15 min at 4°C to collect the pellet containing the isolated mitochondria. The supernatant (cytosolic fraction) was stored at −80°C and the pellet (mitochondrial fraction) was washed and centrifuged at 12,000 × g for 5 min with 500 μL of Mitochondria Isolation Reagent C for purification.

The cell membrane fraction was isolated by using a membrane protein extraction kit (89842, Thermo Fisher Scientific, MA, USA) according to the manufacturer's instructions. In brief, the cellular pellets from approximately 1×10^7 AC16 cells were washed, minced, and suspended in 4.0 mL of cell wash solution. Then, the suspension was homogenized via ten strokes with a prechilled Dounce homogenizer in 1.0 mL of permeabilization buffer, transferred to a new tube, and incubated for 10 min at 4°C in an additional 1.0 mL of permeabilization buffer with constant mixing. The homogenate was centrifuged at 16,000 × g for 15 min at 4°C to collect the pellet, which was the cell membrane fraction. The purity of the fractions was analyzed by immunoblotting with antibodies against GAPDH (cytosolic), COX IV (mitochondrial) and Na, K-ATPase (cell membrane).

Transmission electron microscopy
Heart tissues, AC16, and HEK293T cells with the indicated treatments were dissected into ultrathin sections (70–80 nm) using an ultramicrotome (RMC MT6000-XL). All sections were stained with lead citrate and uranyl acetate and detected under a transmission electron microscope (HT7700, HITACHI, Japan).

Antibodies
All antibodies for Western blot analysis, oligomeric state detection, and immunoprecipation detection used in this study are listed in Table S6.

Western blot analysis
Proteins were extracted from the left ventricular tissue, cardiomyocytes, HEK293T cells, and subcellular fractions with SDS lysis buffer (P0013G, Beyotime Biotechnology, Wuhan, China) containing 1% protease inhibitor (CW2200S, Cowin Biotech, Beijing, China). The protein concentration was quantified with a BCA assay kit (KGP903; KeyGEN BioTECH; Nanjing, Jiangsu, China). Equal quantities of protein extracts were separated by 6%–15% SDS–PAGE and performed by standard western blotting. Protein expression was quantified using Image Lab 3.0 software (Bio-Rad, California, USA) and ImageJ software (National Institutes of Health, Bethesda, Maryland, USA). The total and plasma proteins were normalized to GAPDH, and mitochondrial proteins were normalized to COX IV.

Blue Native-PAGE (BN-PAGE)
BN-PAGE was used to detect mitochondrial membrane oligomers from HEK293T cells, cardiomyocytes, and heart tissue homogenates.[84] Mitochondrial fractions were prepared using a NativePAGE Sample Prep Kit (BN2008, Thermo Fisher Scientific, Waltham, MA, USA) according to the manufacturer's instructions. The lysis buffer contained 1% digitonin to preserve monomeric states as the loading control for oligomeric forms (Chin et al., 2018; Ma et al., 2014). The protein samples were separated by 4%–16% acrylamide gradient gels (BN1004BOX, Thermo Fisher Scientific, Waltham, MA, USA). The gels were electrophoresed in cathode buffer B (50 mM Tricine, 7.5 mM imidazole, 0.02% Coomassie Blue G-250, pH 7.0) and cathode buffer B/10 (50 mM Tricine, 7.5 mM imidazole, 0.002% Coomassie Blue G-250, pH 7.0). Cathode buffer B was replaced with cathode buffer B/10 (with a lower concentration of Coomassie Blue) when the dye front was one-third of the way through the resolving gel. The proteins on the gels were transferred to PVDF membranes in native-PAGE transfer buffer containing 50 mM tricine and 7.5 mM imidazole at 0.2 A for 1 h. The blots were destained in 25% methanol and 10% acetic acid and washed with PBST prior to immunoblotting. COXIV or SDHA as the membrane fraction controls for mitochondria and Na, K-ATPase as a control for cell membrane fraction were used according to previous studies.[85,86]

Co-immunoprecipitation (co-ip) assays
For the analysis of the mitochondrial membrane oligomers, mitochondrial samples from AC16 cells, HEK293T cells, and heart tissue were lysed with cold RIPA buffer (20 mM Tris-HCl pH 7.4, 150 mM NaCl, 1% Triton X-100, 1% NP-40, 0.25% deoxycholate)(P0013D, Beyotime Biotechnology, Wuhan, China) containing 1× protease inhibitor and 1× phosphatase inhibitor (CW2383S, Cowin Biotech, Beijing, China) according to a previous study.[86] The lysed samples were centrifuged at 10,000 × g for 10 min. The 30 μL supernatants were boiled with 1× SDS loading buffer for input prior to SDS–PAGE analysis. The rest of the supernatants (100 μL) was precleared at 4°C for 30 min with 1.0 μg of the control normal anti-mouse IgG (sc-2025, Santa Cruz Biotechnology) together with 20 μL of the resuspended volume of Protein A/G PLUS-Agarose (sc-2003, Santa Cruz Biotechnology, California, USA). The pellet beads were centrifuged at 1,000 × g for 5 min at 4°C. Half of the supernatants were incubated with 2.0 μg of anti-mouse GSDMD (sc-393581, Santa Cruz Biotechnology, California, USA) and 2.0 μg of control normal mouse IgG antibody at 4°C for 1 h, respectively. Then, the above mixtures were incubated with 20 μL of Protein A/G-agarose beads on a rotating device at 4°C for 18 h. The immunoprecipitation beads were washed with cold RIPA buffer for four times and solubilized with 2×NativePAGE Sample Buffer containing 1% n-dodecyl-β-D-maltoside prior to BN-PAGE analysis.

For NLRP3 ubiquitination, total cellular proteins from AC16 cells with the indicated treatments were extracted using cold RIPA buffer as described above, incubated with protein A/G magnetic beads and then immunoprecipitated with 2.0 μg of anti-mouse NLRP3 (ab263899, abcam, Cambridge, MA, USA) or 2.0 μg of control normal rabbit IgG antibody (ab172730, abcam, Cambridge, MA, USA) at 4°C on a rotating device overnight. The eluted proteins were analyzed by Western blotting with the anti-Ub antibody (sc-8017, 1:200) and anti-NLRP3 antibody (ab263899, 1:1000).

QUANTIFICATION AND STATISTICAL ANALYSIS

The results are expressed as the mean ± standard error of the mean (SEM). All statistical analyses were performed using GraphPad Prism 8.0 software. The normality of the data was first determined by the Shapiro-Wilk test. For data that passed the normality test, analyses were performed using a 2-tailed Student's t-test for comparisons between 2 groups, while one-way ANOVA, two-way ANOVA, and multi-factor ANOVA followed by Bonferroni post hoc analysis were applied for comparisons among three or more groups. For nonnormally distributed data, analyses were performed using the Mann–Whitney test for two-group comparisons and Kruskal-Wallis followed by the Dunn post hoc multiple comparisons test for multigroup comparisons. Survival was analyzed by the log rank test and presented as Kaplan–Meier curves. $p < 0.05$ was considered to be a statistically significant difference. All the statistical analyses were performed by an investigator blind to the allocation of treatment and genotype.